Performance Evaluation of an Integrated Floating Energy System Based on Coupled Analysis

Yang YANG [a, b], Musa BASHIR [a], Jin WANG [a], Jie YU [b], Chun LI [b]

[a.] Department of Maritime and Mechanical Engineering, Liverpool John Moores University, Liverpool, Byrom Street, L3 3AF, UK

[b.] School of Energy and Power Engineering, University of Shanghai for Science and Technology, Shanghai, 200093, P.R. China

Abstract: An integrated floating energy system consisting of different types of energy devices is an ideal option for reducing the levelized cost of energy by enhancing the power production capacity. This study proposes a concept of an integrated energy system by combining two tidal turbines with a floating wind turbine. In order to investigate the power performance and dynamic responses of the hybrid concept, a novel coupled aero-hydro-servo-elastic tool is developed based on a commercial hydrodynamic analysis software package. In addition, a torque-pitch controller and the AeroDyn module are integrated within the coupled tool for evaluating the power performance of the tidal turbines under dynamic inflow conditions. Experimental data and numerical results obtained by OpenFAST are used to verify the accuracy of the coupled tool in predicting dynamic responses of the integrated energy system. The dynamic responses and power production under different environmental conditions are obtained by conducting a series of simulations. The results indicate that the total power production is increased by 3.84% to 6.46%. The transient behavior of the platform is improved and the tension fluctuation in mooring lines are significantly reduced by the hydrodynamic damping provided by the tidal turbines. In addition, the tidal turbines have no negative influences on the aero-elastic responses and power performance of the wind energy system. The results have demonstrated the advantages of the integrated energy system in enhancing the power production and improving the dynamic performance.

Keywords: Integrated energy system; Floating wind turbine; Tidal turbine; Coupled model; Dynamic responses; Power production.

1 Introduction

Societal demand for improvements in climatic conditions requires the use of low emission energy sources to mitigate the greenhouse gases effect on the environment. Development of renewable energy resources offers the most efficient means of reducing carbon emissions resulting from the consumptions of fossil energy resources [1]. Offshore renewable energy resources are increasingly attracting attention to meet the growing demand of green energy development. Consequently, the floating energy technology has become a new theme of interest to academic research and commercial development due to the abundance of wind, wave and current resources in the deep sea areas.

Wind energy is the major contributor to the offshore energy development. The past decade has witnessed the conceptualization and commercial application of a number of floating platforms for wind energy exploration. Statoil developed a spar platform, the so-called Hywind concept [2], for the world's first full-scale large floating offshore wind turbine (FWT) with a capacity of 2.3 MW, which became operational in the North Sea, near Norway in 2009. The Hywind concept was adapted by the National Renewable Energy Laboratory (NREL) to support a 5 MW wind turbine in the Offshore Code Comparison Collaboration (OC3) project sponsored by the International Energy Agency (IEA) [3]. Due to its modelling simplicity and commercial viability, the OC3-Hywind was extensively used in a large number of studies in the development of floating wind technology. For instance, Karimirad and Moan [4] analyzed the global dynamic responses of a 5 MW wind turbine supported by a spar platform under harsh environmental and operating conditions. It was found that the dynamic and structural responses were independent of the wind turbulence. Ma *et al.* [5] employed a widely-used numerical analysis tool, FAST, to investigate the dynamic responses of the OC3-Hywind concept under different sea states. The spectral responses were presented to obtain a better understanding of the floating wind turbine's behaviour. Yue *et al.* [6] investigated the effects of heave plates on

the dynamic responses of the spar FWT using AQWA. It was found that the platform motion

was affected by the vertical position of the heave plate. Ahn and Shin [7] conducted various

experimental tests for the OC3-Hywind FWT with a 1/128 scale ratio. The model test results

were compared with the predictions from an in-house code and FAST. It was observed that the

numerical predictions of platform pitch were slightly larger than the test results. Lin *et al.* [8]

investigated the hydrodynamic responses of the OC3-Hywind concept influenced by the

mooring system that was modelled using a quasi-static method. The contributions of mooring

loads to the platform motions were studied. Lyu *et al.* [9] investigated the effects of wind/wave

incident directions of the OC3-Hywind platform responses. It was concluded that the

wind/wave loads significantly affected the longitudinal modes of surge and pitch motions. In

addition, NREL further developed a semi-submersible platform as an alternative floating wind

system in the DeepCwind project [10]. In order to generate sufficient and valid experimental

data for validating and improving the current numerical analysis methodologies for coupled

modelling of FWTs, a series of model tests were conducted for the OC3-Hywind, semi-

submersible and a tension leg platform (TLP) concepts [11]. Dynamic responses and fatigue

damage of the blades and tower of the NREL 5 MW wind turbine supported by three different

types of floating platforms were quantitatively compared [12].

Apart from the offshore wind resource, sea current is also increasingly attracting attention

as an alternative sustainable resource for electricity production. Similar to the wind energy

devices, the most popular design concept of current/tidal turbines is the horizontal axis form

[13]. Patel *et al.* [14] conducted experimental tests to investigate the hydrodynamic

performance of various Darrieus turbines. The solidity effect on the power performance of the

hydrokinetic turbines was studied. It was found that the power coefficient of the turbines with

a symmetric aerofoil achieved their peak at a solidity close to 0.38. In addition, Patel *et al.* [15]

conducted an experimental study to enhance the hydrodynamic performance of a Darrieus

turbine using a blocking plate. The width and location of the blocking plate were tested. The power coefficient of the tidal turbine was increased from 0.125 to 0.36 using an optimal blocking plate. Blackmore *et al.* [16] investigated the effect of turbulence on the power performance and fatigue loads on blades of a tidal turbine through experimental tests. The experiments indicated that the thrust and torque of the tidal turbine were significantly influenced by the dynamic inflow velocity. Scarlett *et al.* [17] carried out a parametric study for a range of flow conditions to investigate the unsteady hydrodynamic performance of tidal turbine blades. It was found that load fluctuations from the blades increased due to a yaw misalignment. Bahaj [18] compared the numerical results obtained using a commercial code with the experimental data. The comparison indicated that the blade element momentum (BEM) theory was able to produce satisfactory representations of the experimental turbine's performance. Zhang *et al.* [19] investigated the hydrodynamic performance of a tidal turbine which was attached on a floating platform. The numerical results indicated that the surge motion had a significant influence on the dynamic performance of the tidal turbine. Patel *et al.* [20] studied the effect of overlap ratio and aspect ratio on the performance of a Savonius-type hydrokinetic turbine through experimental tests. The best overlap and aspect ratios were specified for the purpose of obtaining a maximum energy harvesting efficiency. Patel *et al.* [21] developed a theory based on stagnation pressure and impulse momentum principle for estimating the hydrodynamic performance of a Savonius turbine. The numerical predictions were compared with the data from experimental tests for the validation.

In deep sea areas where wind and current resources coexist, a hybrid energy system consisting of a FWT and several tidal turbines is a prospective and feasible solution to reducing the levelized cost of electricity (LCoE) by sharing the support system. A number of studies have been conducted to investigate the dynamic responses and power production of a hybrid floating energy system. Muliawan *et al.* [22] investigated the dynamic responses and power

106   performance of a combined spar FWT and coaxial floating wave energy converter (WEC) using

107   SIMO/TDHMILL3D. The power take-off system between the WEC and spar platform was

108   modelled as a simple spring-damper. The numerical simulation results of the combined concept

109   under several operating conditions indicated that the fluctuations in the platform motions

110   decreased. The total output power increased by 6% to 15% depending on the environmental

111   conditions. Wan *et al.* [23] conducted an experimental study on the same model under survival

112   conditions to further confirm the deployment feasibility of the combined concept. The test

113   results conformed the accuracy of the numerical modelling in predicting the dynamic responses.

114   A slamming model was suggested to be added into the numerical model to consider the

115   slamming effects which were observed in the tests. Michailides *et al.* [24] studied the dynamic

116   responses and functionality of a semi-submersible wind turbine combined with flap-type wave

117   energy converters through experimental tests and numerical analysis. The results indicated that

118   the combined concept performed well in extreme environmental conditions and no strong

119   nonlinear phenomena were produced [25]. Michele *et al.* [26] developed a mathematical model

120   to study the hydrodynamics of a hybrid wind-wave energy system. The power production

121   capabilities of the hybrid system in regular and irregular wave conditions were investigated.

122   Hallak *et al.* [27] numerically and experimentally analyzed the performance of a combined

123   concept composed of a semi-submersible wind platform and a number of oscillating wave

124   columns. It was found that the hybrid concept benefitted with stability enhancement and

125   smoother energy output. Li *et al.* [28] investigated the dynamic response and power production

126   of a floating energy system consisting of wind, wave and tidal energy devices. It was found

127   that the overall power production increased compared to a single FWT. In addition, the

128   transient behavior following an emergency shutdown was more moderate due to the presence

129   of wave and tidal energy systems. The short-term [29] and long-term [30] extreme responses

130   of the integrated energy system were further studied. It was found that the fatigue damage of

131 mooring lines increased. However, the elasticity of the flexible elements including the blades

132 and tower of the wind turbine was ignored in modelling the hybrid energy system. Moreover,

133 no servo-control scheme was applied to adjust the blade-pitch and rotor speed when evaluating

134 the power production in their studies. It is apparent that the dynamic responses and power

135 performance of such an integrated energy system have not been adequately evaluated.

136   In order to more accurately investigate the dynamic responses and power performance of

137 an integrated floating energy system (IFES), this study has developed a fully coupled aero-

138 hydro-servo-elastic tool based on a commercial hydrodynamic analysis software package,

139 AQWA. The examined IFES concept is composed of a 5 MW spar-type FWT and two 550 kW

140 tidal turbines. In addition, the AeroDyn module developed by NREL is integrated within the

141 coupled tool to predict the hydrodynamic forces produced by the tidal turbines. The influence

142 of platform motions on the relative current speed is considered. The accuracy of the fully

143 coupled tool in predicting dynamic responses of the FWT and tidal turbine is validated through

144 comparisons against OpenFAST and experimental tests, respectively. The coupled dynamic

145 responses of the blades, platform and mooring lines of the IFES under below-rated, rated and

146 over-rated operating conditions are obtained and compared with those of a single FWT. The

147 power production capacity of the IFES is also evaluated to confirm the benefits produced by

148 integrating the tidal turbines with a wind energy system.

149

150 **2 Description of the integrated floating energy system**

151   The IFES model proposed in this study is composed of the NREL 5 MW wind turbine [31]

152 and two identical tidal turbines. Both the wind turbine and tidal turbines are integrated on the
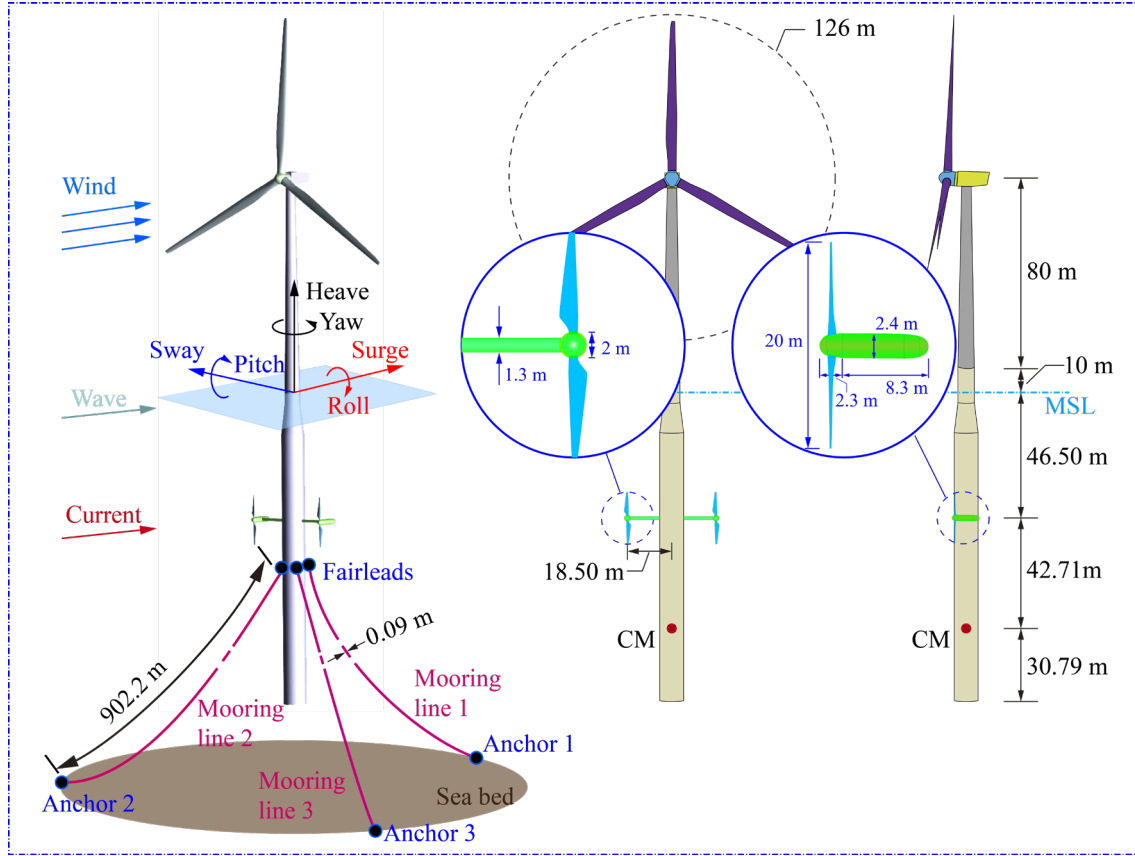
153 spar platform as shown in Fig. 1.

Fig. 1: Schematic diagram of the integrated floating energy system

The extensively-used OC3-Hywind spar [3] is chosen as the main floating component of the IFES concept. The design water depth and total draft of the spar are 320 m and 120 m, respectively. The geometry of the spar near the free-surface is tapered to facilitate a better connection with the tower of the wind turbine. The diameters of the spar above and below the taper are 6.5 m and 9.4 m, respectively. A mooring system consisting of three catenary lines is used for the station-keeping of the platform. The fairleads are attached on the platform at 70 m water depth and the radius of the anchors is 853.87 m. The unstretched length and mass density of each mooring line are 902.2 m and 77.7 kg/m, respectively. The axial stiffness and equivalent weight in water of each mooring line are 384,243,000 N and 698.094 N/m, respectively. The additional yaw stiffness provided by the mooring system is 9.834×10^7 Nm/rad.

The tidal turbine was designed by the Sandia National Laboratory for the development of

marine hydrokinetic technology [32]. The diameters of the rotor and hub are 20 m and 2 m, respectively. The NACA 63-424 aerofoil was used to design the hydrodynamic shape of the rotor blades through an optimization tool named HARP_Opt tool. In this study, the rated rotor speed is increased from 11.5 rpm to 13 rpm to achieve the design power of 550 kW under the rated current speed of 2.0 m/s. Main specifications of the tidal turbine are presented in Table 1 and the hydrodynamic shape of the blade is presented in Table 2.

Table 1: Main specifications of the tidal turbine [32]

Property	Value	Unit
Rated power	550	kW
Cut-in/cut-out current speed	0.5/3.0	m/s
Cut-in/rated rotor speed	3.0/13.0	rpm
Diameter of the rotor	20.0	m
Diameter of the hub	2.0	m
Rotor mass	1200	kg
Nacelle mass	40,100	kg
Cross-beam mass	20,000	kg
Drivetrain inertia moment	4.44×10^6	kg·m^2
Depth to hub below MSL	46.5	m
Distance to hub from centreline of the platform	18.5	m

Table 2: Hydrodynamic shape of the tidal turbine blade [32]

Local radius (m)	Aerofoil (-)	Twist (deg)	Chord (m)	Relative thickness (%)
1.00	Cylinder	12.86	0.800	100.00
1.89	Interpolated	12.86	1.243	53.30
2.70	Interpolated	12.79	1.702	27.55
3.55	NACA 63-424	9.50	1.577	24.00
4.23	NACA 63-424	7.85	1.481	24.00
5.01	NACA 63-424	6.51	1.371	24.00
5.84	NACA 63-424	5.47	1.251	24.00
6.62	NACA 63-424	4.71	1.138	24.00
7.23	NACA 63-424	4.20	1.046	24.00
7.89	NACA 63-424	3.69	0.945	24.00
8.45	NACA 63-424	3.28	0.856	24.00
8.92	NACA 63-424	2.92	0.781	24.00
9.24	NACA 63-424	2.68	0.728	24.00
9.64	NACA 63-424	2.35	0.661	24.00
10.00	NACA 63-424	2.10	0.600	24.00

As indicated in Fig. 1, the tidal turbines are placed at a water depth of 46.5 m. The distance

178   between the tidal turbine's hub and the platform's centerline is 18.5 m. The weight of each

179   tidal turbine including the nacelle and the connecting beam is 6.13×10^4 kg. The added inertial

180   moments of the platform due to the tidal turbines are calculated. By assuming that the ballast

181   of the platform remains unchanged when integrated with the tidal turbines, the inertial

182   properties of the platform are given in Table 3.

183

Table 3: Inertial properties of the platform with the tidal turbines

Property	Value	Unit
Platform mass (with tidal turbines)	7,588,930	kg
Centre of mass (CM) below MSL	89.2141	m
Platform roll inertia about CM	4.46032×10^9	kg·m^2
Platform pitch inertia about CM	4.46032×10^9	kg·m^2
Platform yaw inertia about CM	1.68822×10^8	kg·m^2

184 3 Aero-hydro-servo-elastic modelling of the hybrid concept

185   In order to obtain the dynamic responses of the IFES subjected to wind, wave and current

186   loadings as realistic as possible, an aero-hydro-servo-elastic coupled tool is developed in this

187   study based on a commercial hydrodynamic analysis software tool, AQWA. The aero-servo-

188   elastic simulation capability is implemented within the *user_force64.dll*, which is invoked by

189   the AQWA solver at each time step during a time domain analysis. The kinematics and kinetics

190   of the wind turbine are temporarily stored in the DLL to be used for the simulation in the next

191   time step. The loads calculated by the DLL are coupled with hydrodynamic loads and mooring

192   restoring forces to address the dynamics of the platform and mooring system in the AQWA

193   solver. In addition, the hydrodynamic load of each tidal turbine is calculated using AeroDyn

194   through the DLL, while the dynamic inflow effects due to platform motions are considered.

195   The methodologies used for the development of the aero-hydro-servo-elastic coupled model of

196   the IFES concept are described subsequently. Fig. 2 presents a flowchart of the fully coupled

197   aero-hydro-servo-elastic model established in AQWA. It is apparent that the platform

198   responses obtained using the AQWA solver are influenced by the responses of the wind turbine

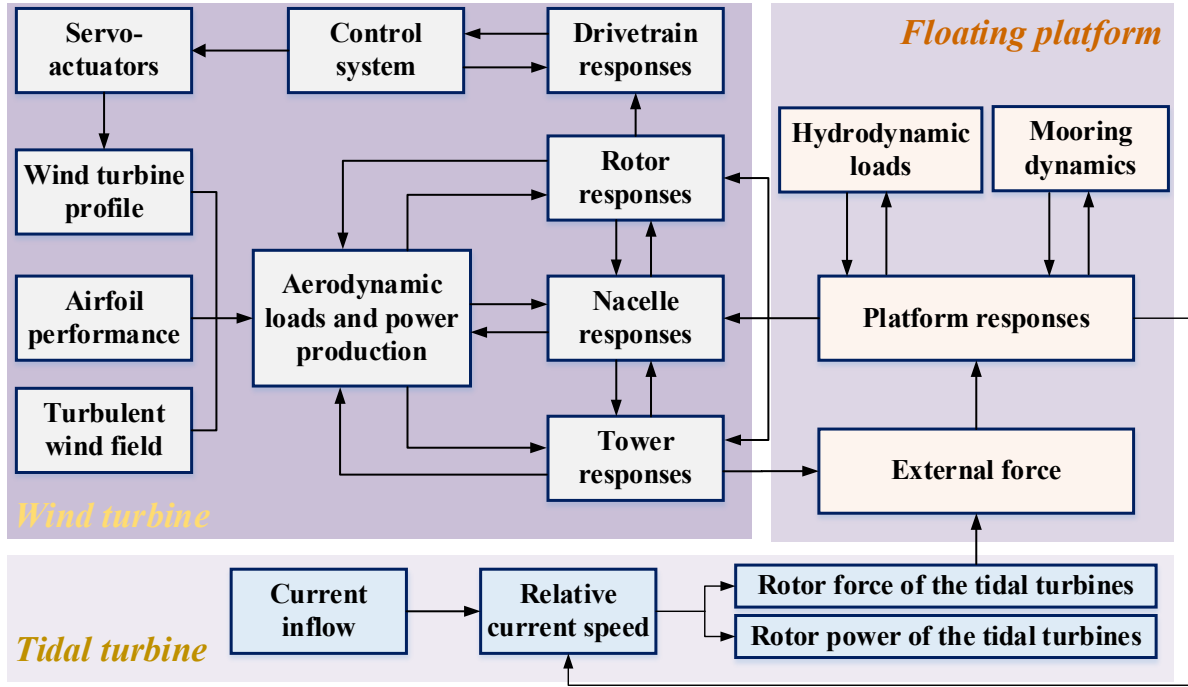199 and tidal turbines predicted in the *user_force64.dll*, and vice versa.

Fig. 2: Flowchart of the fully coupled model for an integrated floating energy system

3.1 Aerodynamic modelling of the rotor

The general dynamic wake (GDW) model and blade element momentum (BEM) [33] theory are adopted to predict the aerodynamic loads of the wind turbine and the hydrodynamic loads of the tidal turbine under a dynamic inflow condition. In the GDW model, the induced velocities and pressure over the rotor disk are solved based on the potential flow theory. By expressing the pressure and induced velocity as infinite series of sines and cosines, the governing equations of the GDW model in the axial and tangential directions are derived in Eq. (1) and Eq. (2), respectively [34].

$$\left[\boldsymbol{M}^{C}\right]\left\{\begin{array}{c}\vdots\\\{\alpha_{j}^{h}\}\\\vdots\end{array}\right\}^{*}+\left[\tilde{\boldsymbol{L}}^{C}\right]^{-1}\left[\hat{\boldsymbol{V}}^{C}\right]\left\{\begin{array}{c}\vdots\\\{\alpha_{j}^{h}\}\\\vdots\end{array}\right\}=\frac{1}{2}\left\{\begin{array}{c}\vdots\\\{\tau_{n}^{mC}\}\\\vdots\end{array}\right\} \tag{1}$$

212
$$\left[\boldsymbol{M}^{S}\right]\left\{\begin{array}{c}\vdots\\\{\beta_{\mathrm{j}}^{\mathrm{h}}\}\\\vdots\end{array}\right\}^{*}+\left[\tilde{\boldsymbol{L}}^{S}\right]^{-1}\left[\hat{\boldsymbol{V}}^{S}\right]\left\{\begin{array}{c}\vdots\\\{\beta_{\mathrm{j}}^{\mathrm{h}}\}\\\vdots\end{array}\right\}=\frac{1}{2}\left\{\begin{array}{c}\vdots\\\{\tau_{\mathrm{n}}^{\mathrm{m}S}\}\\\vdots\end{array}\right\}$$
(2)

213 where $[\boldsymbol{M}^{c}]$ and $[\boldsymbol{M}^{S}]$ are the cosine and sine terms of the apparent mass matrix $[\tilde{\boldsymbol{M}}]$,

214 respectively. $[\tilde{\boldsymbol{L}}^{C}]$ and $[\tilde{\boldsymbol{L}}^{S}]$ are the cosine and sine components of the matrix of inflow gain,

215 respectively. $[\hat{V}^{C}]$ and $[\hat{V}^{S}]$ are the cosine and sine terms of the flow parameters,

216 respectively. $\tau_{\mathrm{n}}^{\mathrm{m}C}$ and $\tau_{\mathrm{n}}^{\mathrm{m}S}$ are respectively the axial and tangential coefficients of

217 dimensionless pressure. $\alpha_{\mathrm{j}}^{\mathrm{h}}$ and $\beta_{\mathrm{j}}^{\mathrm{h}}$ are respectively the axial and tangential coefficients of

218 induced velocity.

219 The induced velocity distribution over the rotor disk is obtained by solving the above

220 differential equations. The Prandtl corrections are used to consider the tip and hub losses. The

221 BEM theory is then used to calculate the loads acting on each blade element based on the lift

222 and drag coefficients of the local sectional aerofoil, as denoted in Eq. (3) and Eq. (4) [35].

223
$$\mathrm{d}T=\frac{1}{2}\rho W^{2}c(C_{l}\cos\phi+C_{d}\sin\phi)\mathrm{d}r$$
(3)

224
$$\mathrm{d}M=\frac{1}{2}\rho W^{2}c(C_{l}\sin\phi-C_{d}\cos\phi)r\mathrm{d}r$$
(4)

225 where dT and dM are, respectively, the thrust and moment of the local blade element; ρ is

226 the density of the inflow fluid; C_{l} and C_{d} are, respectively, the lift and drag coefficients of

227 the sectional aerofoil; The Beddoes-Leishman dynamic stall model is used to correct the

228 aerodynamic coefficients under unsteady conditions; c is the chord length of the blade element;

229 r and dr are the local radius and length of the blade element, respectively; ϕ is the relative

230 inflow angle of the local section; W denotes the relative inflow speed.

231

232 ## 3.2 Structural modelling of the wind turbine

233 The wind turbine is modelled as a multi-body system consisting of rigid and flexible

234   bodies. The hub and nacelle were treated as rigid bodies. The tower and blades were modelled

235   as flexible bodies based on the linear modal approach. For each blade, two flapwise and one

236   edgewise modes are considered. The first two modes in the fore-aft and side-side directions are

237   examined for the tower. In addition, the nacelle-yaw and rotation of the drivetrain system are

238   accounted in the simulation. Kane's method [36] is used to establish the equations of motion

239   of the wind turbine, as follows:

240    $$\boldsymbol{F}_i^* + \boldsymbol{F}_i = 0 \tag{5}$$

241   where $\boldsymbol{F}_i^*$ and $\boldsymbol{F}_i$ are the generalized inertia and active forces corresponding to the ith degree

242   of freedom (DOF) of the wind turbine.

243   The generalized inertia force of a rigid body can be represented using the same formula.

244   For instance, the generalized inertia force of the nacelle $\boldsymbol{F}_{\text{Nac}}^*$ is derived as:

245    $$\boldsymbol{F}_{\text{Nac}}^* = \sum_{i=1}^{N} v_{i,\text{Nac}}(-m_{\text{Nac}} \cdot a_{\text{Nac}}) + \omega_i(-\dot{H}_{\text{Nac}}) \tag{6}$$

246   where N is the number of total examined DOFs of the wind turbine; $v_{i,\text{Nac}}$ is the partial velocity

247   of the nacelle contributed by the ith DOF of the wind turbine; m_{Nac} and a_{Nac} are respectively

248   the mass and acceleration of the nacelle; ω_i is the partial angular velocity of the nacelle

249   contributed by the ith DOF of the wind turbine; $\dot{H}_{\text{Nac}}$ is the time derivative of angular

250   momentum of the nacelle about its mass center.

251   The term, $\omega_i(-\dot{H}_{\text{Nac}})$, denotes the gyroscopic yaw moment induced by the spinning

252   inertia and pitching motion of the rotor. The pitching motion denoted by the partial angular

253   velocity (ω_i) is influenced by the pitching velocities of the tower and platform. An exhaustive

254   description of the relationship between the partial angular velocity of the nacelle and

255   kinematics of tower and platform is beyond the scope of this study. Further details can be found

256   in reference [36]

257   The generalized inertia force of a blade $\boldsymbol{F}_{\text{Bld}}^*$ is denoted as:

$$\boldsymbol{F}_{\text{Bld}}^{*} = -\sum_{i=1}^{N} \int_{0}^{R_{\text{rt}} - R_{\text{hub}}} \rho_{\text{Bld}}(r) \cdot v_{i,\text{Bld}}(r) \cdot a_{\text{Bld}}(r) \cdot \mathrm{d}r \tag{7}$$

where R_{rt} and R_{hub} are the radii of the rotor and hub, respectively; $\rho_{\text{Bld}}(r)$ is the mass of the

blade per unit length; $v_{i,\text{Bld}}(r)$ is the partial velocity of the local blade section contributed by

the ith DOF of the wind turbine; and $a_{\text{Bld}}(r)$ is the acceleration of the local blade section.

The generalized active forces are composed of aerodynamic load $F_{i,\text{aero}}$, elastic restoring

force $F_{i,\text{elastic}}$, gravitational load $F_{i,\text{grav}}$ and damping force $F_{i,\text{damp}}$, as denoted in Eq. (8).

$$F_i = F_{i,\text{aero}} + F_{i,\text{elastic}} + F_{i,\text{grav}} + F_{i,\text{damp}} \tag{8}$$

The generalized active aerodynamic force acting on a blade $F_{\text{Bld,aero}}$ is denoted as:

$$F_{\text{Bld,aero}} = \sum_{i=1}^{N} \int_{0}^{R_{\text{rt}} - R_{\text{hub}}} v_{i,\text{Bld}}(r) \cdot F_{\text{aero}}(r) \cdot \mathrm{d}r \tag{9}$$

where $F_{\text{aero}}(r)$ is the total force acting on the local blade section.

The generalized active elastic restoring force of a blade is defined as a partial derivative

of the potential energy with respect to the generalized coordinate, as follows:

$$F_{\text{Bld,elastic}} = \frac{\partial V_{\text{PE}}}{\partial q_{\text{Bld}}} = \frac{\partial \left[\dfrac{1}{2} \sum_{i}^{n} \sum_{j}^{n} k_{ij} \cdot q_i(t) \cdot q_j(t) \right]}{\partial \left[q_{\text{Bld}}(t) \right]} \tag{10}$$

where V_{PE} is the potential energy of the blade; $q_i(t)$ is the generalized coordinate associated

with the ith mode pertaining to the blade at the time of t; n is the number of the examined modes

of the blade; k_{ij} is the generalized stiffness of the blade and its value is zero when $i \neq j$.

Considering rotational effects of the rotor, the generalized stiffness of a blade is given in

Eq. (11).

$$k_{ij} = \int_{0}^{R_{\text{rt}} - R_{\text{hub}}} EI_{\text{Bld}}(r) \frac{\mathrm{d}^2 \varphi_i(r)}{\mathrm{d}r^2} \frac{\mathrm{d}^2 \varphi_j(r)}{\mathrm{d}r^2} \mathrm{d}r + k_{\text{tm},ij} + k_{\text{lm},ij} \tag{11}$$

where $EI_{\text{Bld}}(r)$ is the distributed stiffness of the blade. $\varphi_i(r)$ is the ith normalized modal

shape of the blade; $k_{\text{tm},ij}$ and $k_{\text{lm},ij}$ are the generalized stiffness due to the tip mass and local

mass of the blade, as derived in Eq. (12) and Eq. (13), respectively.

$$280 \qquad k_{\text{tm},ij} = \Omega^2 m_{\text{tip}} R_{\text{rt}} \int_0^{R_{\text{rt}}-R_{\text{hub}}} \frac{\mathrm{d}\varphi_i(r)}{\mathrm{d}r} \frac{\mathrm{d}\varphi_j(r)}{\mathrm{d}r} \mathrm{d}r \qquad (12)$$

$$281 \qquad k_{\text{lm},ij} = \Omega^2 \int_0^{R_{\text{rt}}-R_{\text{hub}}} \rho_{\text{Bld}}(r)(R_{\text{rt}}+r)\left[\int_0^r \frac{\mathrm{d}\varphi_i(r')}{\mathrm{d}r'} \frac{\mathrm{d}\varphi_j(r')}{\mathrm{d}r'} \mathrm{d}r'\right] \mathrm{d}r \qquad (13)$$

282

283 where Ω and m_{tip} are the rotational speed of the rotor and the tip mass of the blade,

284 respectively.

285   Substituting Eqs. (6)~(13) into Eq. (5), the coupled equation of motion of the wind turbine

286 is established. It is noted that the effects of platform motions on the kinematics of the upper

287 structures including the rotor, nacelle and tower are considered based on the theory described

288 in [37] when solving Eq. (5) in the DLL. The kinetic results obtained from the solutions are

289 passed into AQWA solver through the DLL for the calculation of platform motions at each

290 time step in the analysis. The platform's kinematics obtained from the AQWA solver are then

291 fed back into the DLL for solving Eq. (5) at the next time step.

292

293 *3.3 Integration of the coupled model of the IFES*

294   The aero-servo-elastic model is integrated within a commercial hydrodynamic analysis

295 tool, AQWA, through its built-in DLL (*user_force64.dll*) to form a fully coupled model of

296 IFES. In a time-domain analysis performed in AQWA, the DLL is invoked by the AQWA

297 solver to obtain the external force and added-mass. The aero-servo-elastic simulation capability

298 is implemented within the DLL by fully modifying its source code. The aero-servo-elastic

299 responses of the upper structures are represented by the external force and added-mass during

300 each invocation, and then passed into AQWA solver to be combined with the hydrodynamic

301 loads and mooring restoring forces for obtaining the dynamic responses of the platform. The

302 equation of motion of the platform is derived as follows:

$$303 \qquad (\boldsymbol{m}+\boldsymbol{A}_{\text{wv}}+\boldsymbol{A}_{\text{wt}})\ddot{\boldsymbol{X}}(t)+\boldsymbol{C}\dot{\boldsymbol{X}}(t)+\boldsymbol{K}\boldsymbol{X}(t)+\int_0^t \boldsymbol{h}(t-\tau)\ddot{\boldsymbol{X}}(\tau)\mathrm{d}\tau = \boldsymbol{F}_{\text{h}}(t)+\boldsymbol{F}_{\text{t}}(t)+\boldsymbol{F}_{\text{e}}(t) \quad (14)$$

304   where m is the inertial mass matrix of the platform, A_{wv} is the added-mass matrix due to

305   the wave, A_{wt} is the mass matrix of the upper structures referred to the platform's mass

306   center; K and C are, respectively, the total stiffness and damping matrices; $X(t)$, $\dot{X}(t)$ and

307    $\ddot{X}(t)$ are, respectively, the displacement, velocity and acceleration vectors of the platform;

308    $h(t)$ is the acceleration impulse function matrix used to examine the radiation memory effects;

309    $F_h(t)$ and $F_t(t)$ are, respectively, the total hydrodynamic and mooring load vectors acting

310   on the platform; $F_e(t)$ is the external force vector obtained through the DLL, including the

311   loads from the upper structures and the force acting on the tidal turbine.

312   The hydrodynamic loads acting on the platform are calculated based on the frequency-

313   dependent hydrodynamic coefficients including the added mass, radiation damping and

314   restoring forces, which are obtained from a frequency domain analysis in AQWA. The panel

315   model of the IFES is presented in Fig. 3. Since the blades of the tidal turbines are small

316   components but with a complicated geometry, they have been represented by an equivalent

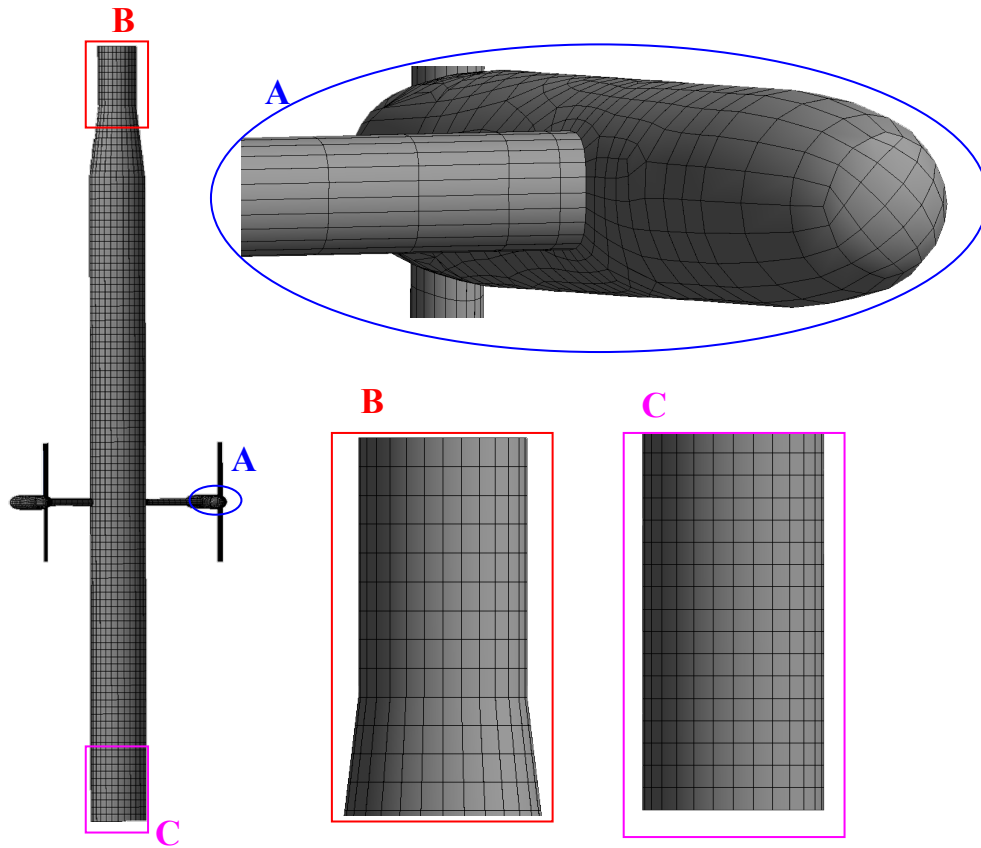317   diameter cylinder for simplicity in performing the frequency domain analysis.

Fig. 3: Panel model of the integrated floating energy system in AQWA

The hydrodynamic force acting on the tidal turbine's rotating rotor due to the inflow current is calculated using AeroDyn. The interaction between the tidal turbines and the platform is examined by considering the relative inflow effects due to the platform motions. In other words, the longitudinal velocity of the tidal turbine is affected by the platform surge, pitch and yaw motion as shown in Fig. 4.
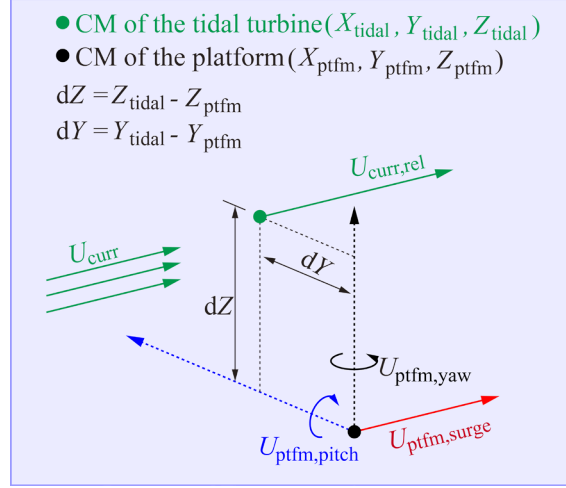
Fig. 4: Velocities of the tidal turbine and platform

Based on the assumption of small rotations of the platform, the actual relative inflow current speed $U_{curr,rel}$ is corrected as follows:

$$U_{curr,rel} = U_{curr} - U_{ptfm,surge} - (Z_{tidal} - Z_{ptfm})U_{ptfm,pitch} + (Y_{tidal} - Y_{ptfm})U_{ptfm,yaw} \qquad (15)$$

where U_{curr} is the defined inflow current speed at the tidal hub depth. $U_{ptfm,surge}$, $U_{ptfm,pitch}$ and $U_{ptfm,yaw}$ are the surge, pitch and yaw velocities of the platform, respectively. Z_{tidal} and Z_{ptfm} are the vertical coordinates of the CMs of the tidal turbine and platform, respectively. Y_{tidal} and Y_{ptfm} are the lateral coordinates of the CMs of the tidal turbine and platform, respectively.

The current speed along water depth follows a power law distribution with an exponent of 1/7. At each time step, U_{curr} is calculated according to the hub depth of the tidal turbine and the given current speed at the MSL. A variable-speed and variable-pitch controller is implemented based on the control algorithm proposed by Jonkman [31] for the NREL 5MW wind turbine. The power and torque performance of the tidal turbine subjected to different steady inflow current speeds are evaluated in order to obtain the proportional and integral gains. Appendix A presents a brief description of the implementation method of the controller for the

344   tidal turbine.

345   It is noted that the results directly produced by the AQWA solver and the DLL are referred

346   to different coordinate systems. The tower-base loads referred to the platform's local

347   coordinate system need to be converted to the external force referred to the inertial coordinate

348   frame. In addition, the external forces are applied at the platform's CM. Similarly, the platform

349   motions used to correct the kinematics of the blades and tower need to be converted from the

350   inertia coordinate system to its local coordinate frame. The matrix, $\mathbf{T}_{\text{mat}}$, given in Eq. (16) is

351   used to achieve accurate transformations on the platform kinematics and external forces.

352
$$\mathbf{T}_{\text{mat}} = \begin{bmatrix} \dfrac{\theta_1^2\sqrt{1+s}+\theta_2^2+\theta_3^2}{s\sqrt{1+s}} & \dfrac{\theta_3 s+\theta_1\theta_2(\sqrt{1+s}-1)}{s\sqrt{1+s}} & \dfrac{-\theta_2 s+\theta_1\theta_3(\sqrt{1+s}-1)}{s\sqrt{1+s}} \\[3ex] \dfrac{-\theta_3 s+\theta_1\theta_2(\sqrt{1+s}-1)}{s\sqrt{1+s}} & \dfrac{\theta_2^2\sqrt{1+s}+\theta_1^2+\theta_3^2}{s\sqrt{1+s}} & \dfrac{\theta_1 s+\theta_2\theta_3(\sqrt{1+s}-1)}{s\sqrt{1+s}} \\[3ex] \dfrac{\theta_2 s+\theta_1\theta_3(\sqrt{1+s}-1)}{s\sqrt{1+s}} & \dfrac{-\theta_1 s+\theta_2\theta_3(\sqrt{1+s}-1)}{s\sqrt{1+s}} & \dfrac{\theta_3^2\sqrt{1+s}+\theta_1^2+\theta_2^2}{s\sqrt{1+s}} \end{bmatrix} \qquad (16)$$

353   where θ_1, θ_2 and θ_3 are, respectively, the roll, pitch and yaw angles of the platform. s is

354   equal to $\theta_1^2+\theta_2^2+\theta_3^2$.

355   By setting the platform reference point as the origin of the inertial coordinate system in

356   establishing its local coordinate frame, the platform position vector is corrected as follows:

357
$$\mathbf{D}_{\text{DLL}} = \mathbf{D}_{\text{AQWA}} - \mathbf{T}_{\text{mat}} \cdot \mathbf{CoG} \qquad (17)$$

358   where $\mathbf{CoG}$ is the position vector from the reference point to the platform's CM. $\mathbf{D}_{\text{AQWA}}$

359   and $\mathbf{D}_{\text{DLL}}$ are the platform displacement vectors obtained in AQWA and the one passed into

360   the DLL, respectively.

361   The translational velocity vector of the platform is corrected as follows:

362
$$\mathbf{U}_{\text{DLL}} = \mathbf{U}_{\text{AQWA}} - \mathbf{T}_{\text{mat}} \cdot \mathbf{CoG} \times \boldsymbol{\omega} \qquad (18)$$

363   where $\mathbf{U}_{\text{AQWA}}$ and $\mathbf{U}_{\text{DLL}}$ are the platform velocity vectors obtained in AQWA and the one

364   used in the DLL, respectively; $\boldsymbol{\omega}$ is the rotational velocity vector of the platform obtained in

365   AQWA.

366   Since the fourth-order Adams-Beshforth-Mounton predictor-corrector method is used to

367   solve the equation of motion given in Eq. (5), the accelerations of the involved structures are

368   needed. However, the platform acceleration is not permitted to be shared with the DLL.

369   Therefore, the platform acceleration vector is estimated numerically in the DLL based on the

370   velocity vectors at the last and current time steps as follows:

371
$$\mathbf{a}_{DLL} = (\mathbf{U}_{DLL} - \mathbf{U}'_{DLL}) \big/ \Delta t \tag{19}$$

372   where $\mathbf{a}_{DLL}$ is the platform acceleration and $\mathbf{U}'_{DLL}$ is the platform velocity at the last time

373   step, Δt is the time step of the simulation.

374   Similarly, the tower-base loads obtained directly in the DLL are transformed as follows:

375
$$\mathbf{F}_{AQWA} = \mathbf{T}_{mat}^{-1} \cdot \mathbf{F}_{DLL} \tag{20}$$

376
$$\mathbf{M}_{AQWA} = \mathbf{T}_{mat}^{-1} \cdot (\mathbf{M}_{DLL} - \mathbf{CoG} \times \mathbf{F}_{DLL}) \tag{21}$$

377   where $\mathbf{F}_{AQWA}$ and $\mathbf{F}_{DLL}$ are the translational force vectors in the AQWA program and DLL,

378   respectively. $\mathbf{T}_{mat}^{-1}$ is the inverse matrix of $\mathbf{T}_{mat}$. $\mathbf{M}_{AQWA}$ used in AQWA is the moment

379   vector acting at the platform's mass center with respect to the inertial coordinate system. $\mathbf{M}_{DLL}$

380   obtained in the DLL is the moment vector acting at the tower-base with respect to the platform's

381   local coordinate system.

382

383 **4 Validation of the fully coupled model**

384   Since there is no credible model test or numerical data available for the full IFES model

385   adopted in this study, the validation of the aero-hydro-servo-elastic coupled model is conducted

386   in two parts: (i) to validate the accuracy of the fully coupled model in predicting dynamic

387 responses of a FWT by comparing it with OpenFAST; (ii) to confirm that hydrodynamic

388 performance of a tidal turbine can be evaluated credibly; the results from the model tests by

389 Bahaj *et al.* [38] and Doman *et al.* [39] are used in the comparisons. In addition, the results of

390 the tidal turbine under steady inflow conditions are compared with its design parameters to

391 verify the controller.

4.1 Accuracy in predicting fully coupled responses of the wind turbine

393 FAST was developed by NREL for aero-hydro-servo-elastic coupled analysis of

394 horizontal axis wind turbines. FAST has been verified and approved as credible numerical tool

395 for the analysis of wind-wave coupled loads on wind turbines by Germanischer Lloyd. In

396 addition, FAST was used as the main numerical tool in numerous international projects

397 including the OC3 project, a collaborative research with focus on validation and improvement

398 of numerical tools for wind turbine analysis. The numerical predictions from FAST agreed well

399 with the experimental data for the OC3-Hywind [40] and DeepCwind semi-submersible [41]

400 concepts. Since FAST has been well validated by experimental data in numerous studies, it is

401 agreed that the tool is capable of producing accurate and reliable numerical results for

402 simulations of FWTs under wind-wave coupled conditions. OpenFAST, the latest version of

403 FAST, is therefore used to validate the coupled model developed in this study.

404 Since the process of generating an irregular wave in AQWA and OpenFAST is different,

405 the examined met-ocean condition is composed of a regular wave and a turbulent wind. The

406 turbulent wind has an average speed of 11.4 m/s at the hub height and a shear exponent of 0.12.

407 The wave height and period are, respectively, 1.94 m and 5.01 s. The coupled responses of the

408 platform are compared in Fig. 5. Although a notable difference is observed, the platform surge

409 motion predicted by the coupled model in AQWA follows the same trend as the results obtained

410 using OpenFAST. The average surge motions of AQWA and OpenFAST are 20.7 m and 20.9

411 m, respectively. The discrepancy between the heave motions is relatively smaller than the

difference in the surge motion. The heave motion predicted by the coupled model developed in AQWA is almost identical with the result obtained using OpenFAST. The agreement between AQWA and OpenFAST is reasonably good in predicting the platform pitch motion. The results predicted by these two tools follow the same trend over the simulation, although minor differences are observed. The average platform pitch motions from AQWA and OpenFAST are 4.24 degrees and 4.33 degrees, respectively. The relative difference is around 1.92%. The differences between the results are mainly attributed to the mooring system and hydrodynamic loads. Each mooring line is modelled as a quasi-static catenary in OpenFAST, while the mooring lines are modelled using a dynamic approach in AQWA to examine the dynamic effects of the platform motions. In addition, some differences between these two tools in predicting hydrodynamic loads exist. For example, the duration of the convolutional integral used to calculate the radiation force due to memory effect is 120 s in AQWA, while the memory duration in OpenFAST is 60 s by default. Nonetheless, the differences between the platform motions obtained using AQWA and OpenFAST are negligible.
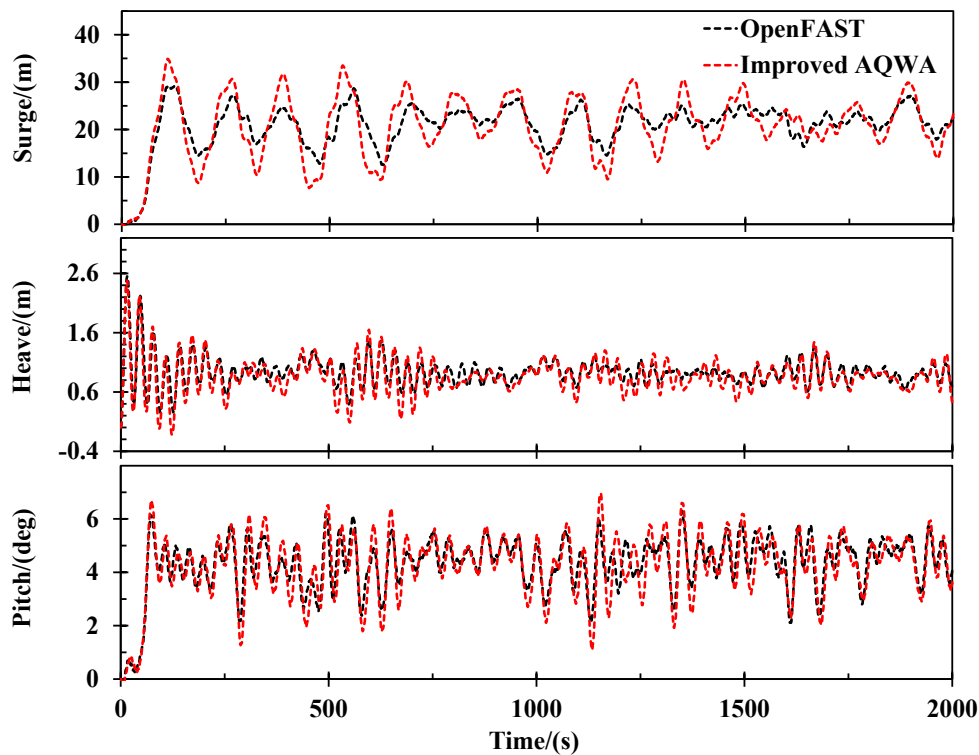
427   Fig. 5: Comparison between platform responses obtained using OpenFAST and the present
428   coupled model developed in AQWA.

429

430   Fig. 6 presents the fairlead tension of each mooring line obtained using OpenFAST and

431   the present coupled model developed in AQWA. The agreement between the fairlead tensions

432   predicted by these two tools is good for each of the mooring lines. The small discrepancy is

433   attributed to the difference in modelling the mooring lines in AQWA and OpenFAST. Each

434   mooring line is modelled as a quasi-static catenary in OpenFAST, while the mooring lines are

435   modelled as dynamic catenaries in AQWA. The dynamic effects due to platform motions are

436   examined in AQWA. Consequently, the tension in each mooring line predicted by AQWA

437   fluctuates in a relatively larger range compared to the results obtained using OpenFAST.

438   Nonetheless, the differences between the mooring tensions obtained using AQWA and

439   OpenFAST are acceptable. The comparisons against OpenFAST indicate that the aero-hydro-

440   servo-elastic model that has been well implemented within AQWA is capable of accurately

441   predicting coupled responses of the FWT. The DLL is capable of performing a fully coupled

442   analysis in AQWA and it has been released to the public on an open source platform, GitHub,
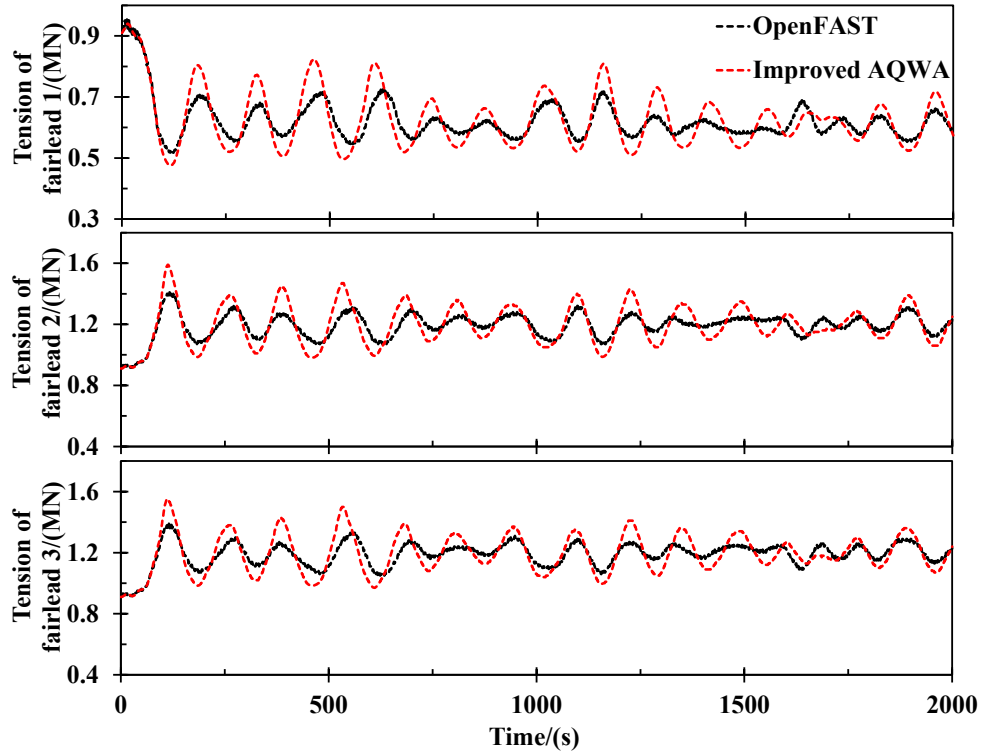
443   as shown in Appendix B.

Fig. 6: Fairlead tension of each mooring line predicted by OpenFAST and the present coupled model developed in AQWA.

4.2 Credibility in evaluating hydrodynamic performance of the tidal turbine

The model tests conducted by Bahaj *et al.* [38] and Doman *et al.* [39] are used to validate

the numerical tool integrated within AQWA. Fig. 7 presents the comparisons between the test

data and numerical results for two different tidal turbines. It is observed that the power and

thrust coefficients predicted in the present numerical simulations follow the same variation

trends as the data from model test 1, although the numerical simulation slightly overestimates

the power coefficient at a high tip speed ratio (TSR). In the model test 2, the numerical results

are slightly higher than the test data for low TSRs. In the common operational range of TSR

between 4 and 6, the power and thrust coefficients predicted by the numerical model agree well

with the test results in both magnitude and variation trend. The overall agreements between the

results of the numerical simulations and model tests are reasonably good. The comparisons

have confirmed the accuracy of the numerical model in predicting responses of tidal turbines.
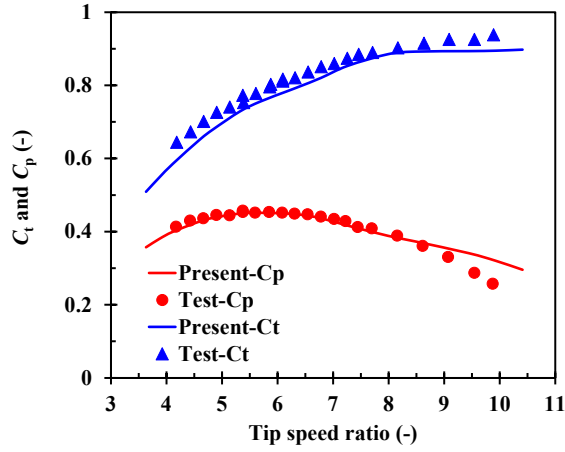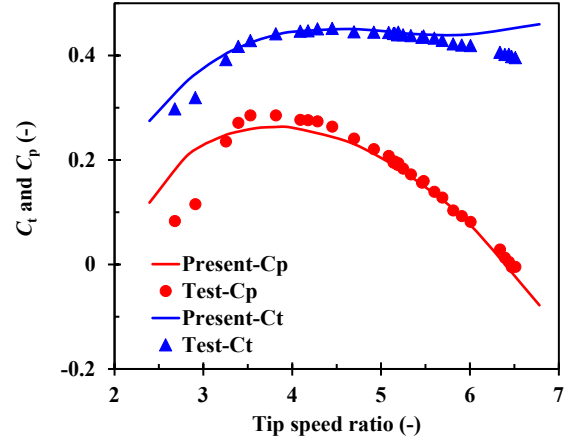
(a) Model test 1　　　　　　　　　　　　　(b) Model test 2

Fig. 7: Comparison between tidal turbine responses obtained from the present numerical simulations and model tests; (a) model test 1 conducted by Bahaj *et al.* [38] for a 0.8 m diameter rotor, (b) model test 2 conducted by Doman *et al.* [39] for a 0.762 m diameter rotor.

For each inflow current speed within the operational range, a simulation with a duration of 800 s is conducted. The first 200 s transient results are removed and the results of the last 600 s are used to obtain the average power and rotor speed. Fig. 8 presents the comparisons between the power and rotor speed predicted by the numerical model and the design parameters versus inflow current speed. It is observed that the numerical results are identical to the design parameters for each inflow current speed. The comparison indicates that the controller implemented in this study is efficient in adjusting rotor speed and blade pitch to achieve a target power.
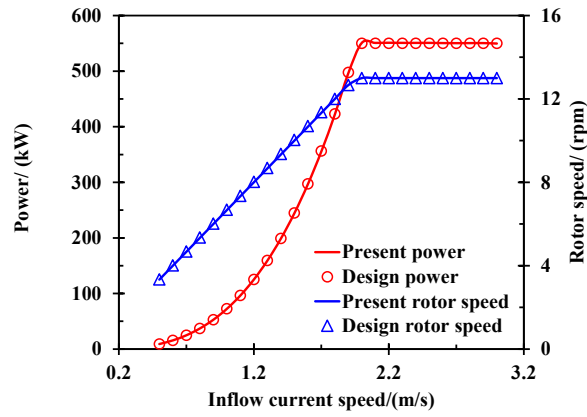
Fig. 8: Comparisons of power and rotor speed under steady conditions

5 Results and Discussions

In this section, the performance of the IFES is evaluated and compared against a single FWT for below-rated, rated and over-rated conditions with regards to the responses of the blades, platform and mooring system. In addition, the power production of these two floating energy systems are compared to highlight the advantage of the IFES concept.

5.1 Load case definition

Based on the met-ocean data of a specific site over the west coast of USA [42], three typical load cases (LCs) are defined. The average wind speeds at the height of 90 m above the MSL are 8 m/s, 11.4 m/s and 16 m/s, respectively, for the three LCs. The corresponding wave properties and current speed at the MSL are presented in Table 4. It is noted that the rated current speed of the tidal turbine is 2 m/s which is much larger than the current speed examined in this study. It is anticipated that the additional power production of the tidal turbines will be less than their rated power. The full-field turbulent winds are generated using TurbSim [43] based on the Kaimal spectrum. A power-law profile with an exponent of 0.12 is adopted to examine the wind shear effect. Fig. 9 presents the generated wind field with an average speed of 11.4 m/s at the hub height. The kinematics of the irregular waves are generated based on the

493   P-M spectrum in AQWA. The current speed distribution along the water depth follows a

494   power-law profile with an exponent of 1/7 as suggested [32]. The dynamic responses of the

495   IFES and FWT are examined for each load case. The simulation length is 4600 s and the time

496   step is 0.005 s.

497   Table 4: Environmental conditions of the load cases

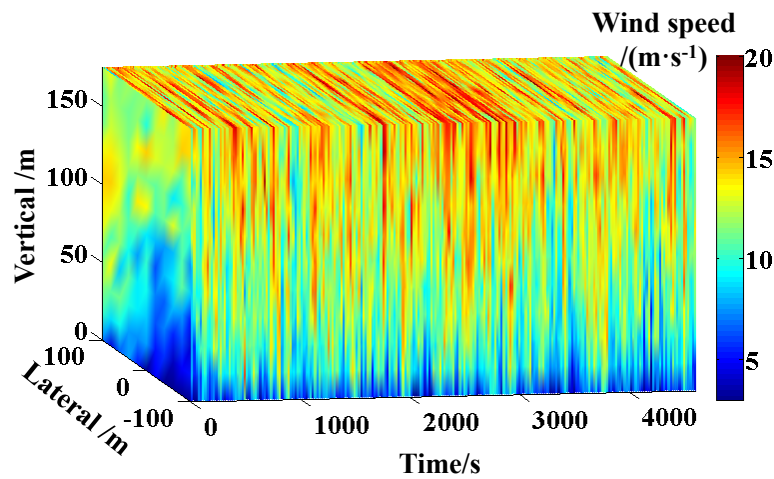| Load case	Wind speed at hub height (m/s)	Significant height (m)	Spectral peak period (s)	Current speed at the MSL (m/s)
LC1	8.0	1.316	8.006	1.0
LC2	11.4	1.836	7.441	1.1
LC3	16.0	2.598	7.643	1.2

498
499   Fig. 9: Wind field with an average speed of 11.4 m/s at the hub height
500

5.2 Blade responses

502   The out-of-plane (OoP) blade-tip deflection and rotor thrust of the present IFES concept

503 and a single FWT under LC2 are presented in Fig. 10. The time domain variations of the rotor

504 thrust of the IFES follows the same trend as the result of the FWT. The difference in magnitude

505 is negligible. Similar phenomenon is observed for the blade-tip deflection. The results indicate

506 that the tidal turbines attached to the spar platform have insignificant effects on the

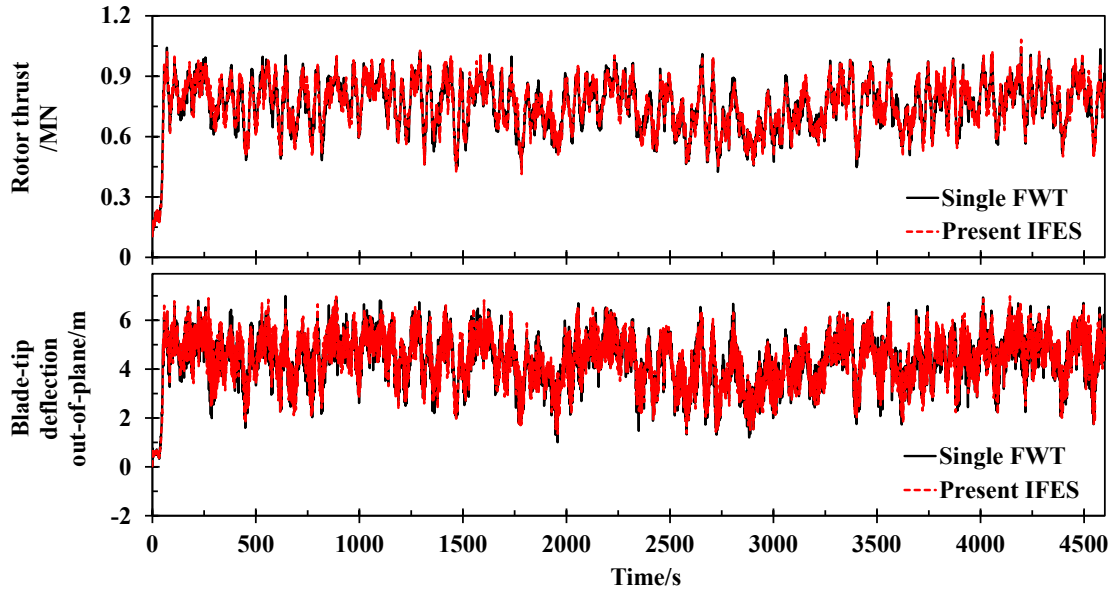507 aerodynamic performance of the wind turbine.

Fig. 10: Blade-tip deflection and rotor thrust under LC2

Table 5 presents the statistics of the blade-tip deflection and rotor thrust of the single FWT and IFES under the three LCs. The maximum blade-tip deflection of the IFES under LC1 is 1.1% smaller than that of the FWT, the corresponding standard deviation is 1.28% larger. Similar phenomenon is observed for the rotor thrust. It is noted that the errors between the statistical responses of the IFES and FWT are smaller than 2% for all the LCs, which include the below-rated and over-rated conditions. The aero-elastic responses and aerodynamic performance of the IFES are similar to those of the FWT. The statistical results imply that the influence of the tidal turbines on the dynamic responses of the rotor is weak. It is anticipated that the installation of additional tidal turbines on the spar platform has negligibly negative effects on the dynamics and performance of the blades.

Table 5: Statistics of the OoP blade-tip deflection and rotor thrust (during 400 s ~ 4600s)

		Blade-tip deflection (OoP)/m			Rotor thrust/kN		
		IFES	FWT	Error	IFES	FWT	Error
	Max	4.58	4.63	-1.10%	733.8	747.7	-1.86%
LC1	Mean	3.27	3.28	-0.20%	554.5	554.5	-0.01%
	Std.dev	0.39	0.38	1.28%	57.7	58.6	-1.44%
LC2	Max	7.00	7.05	-0.62%	1036.0	1052.0	-1.52%
	Mean	4.47	4.45	0.51%	769.1	765.0	0.53%

	Std.dev	0.97	0.99	-1.42%	114.7	117.0	-1.99%
	Max	6.27	6.12	2.42%	1029.0	1016.0	1.28%
LC3	Mean	2.49	2.47	0.82%	558.5	553.5	0.90%
	Std.dev	1.01	1.00	0.92%	95.9	94.7	1.32%

522

5.3 Platform responses

The platform responses of the IFES and the single FWT under LC2 are presented in Fig. 11. Significant differences between the platform motions of the IFES and FWT are observed. The average value of the surge motion of the IFES is significantly larger, while the fluctuation is much smaller compared to the surge motion of the single FWT. This is because the tidal turbines provide a considerable thrust when the wind turbine moves towards the inflow wind. The hydrodynamic thrusts produced by the tidal turbines act as a damping against the wind turbine when moving towards the upwind direction. The presence of the tidal turbines improves the transient behavior of the platform which is caused by the rapid decrease of aerodynamic damping when the controller increases the blade pitch angle under an over-rated condition.

The platform heave of the IFES is smaller than the heave of the FWT. This means that the equilibrium position of the IFES is lower since the buoyancy provided by the tidal turbines is smaller than their weights. Relatively small discrepancy in the pitch motions of the IFES and FWT is observed. The contribution by the tidal turbines to the platform pitch motion is negligible since the pitch motion is mainly influenced by the wind loading. As indicated by the results presented in Fig. 10, the tidal turbines have insignificant effects on the aerodynamic loads of the wind turbine, although they have notable effects on the platform surge that is coupled with aerodynamic loads. However, the velocity variation of the turbulent wind in LC2 is still the main contribution to the fluctuation of relative inflow speed of the wind turbine. Therefore, the pitch motion dominated by the wind loading is weakly affected by the tidal turbines.
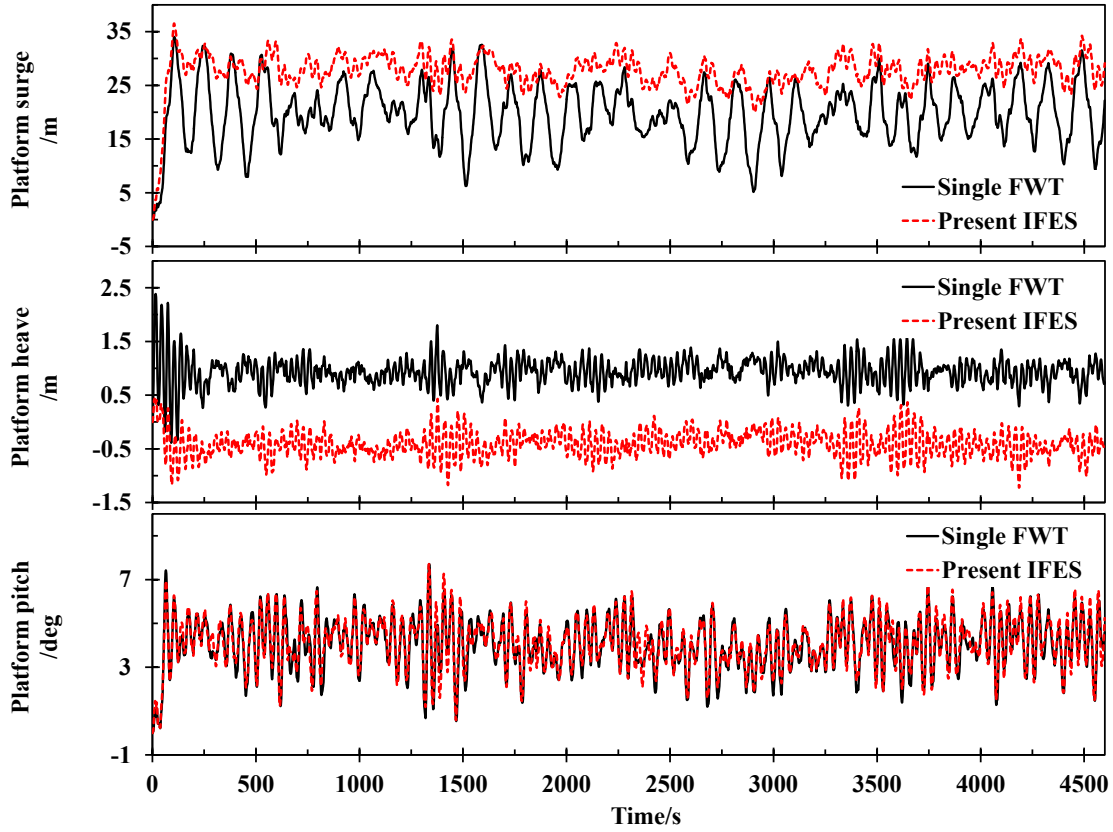
Fig. 11: Platform motions of the IFES and FWT under LC2.

By applying a Fast Fourier Transformation (FFT) on the time series of the platform responses under LC2, the spectral responses of the platform are obtained as presented in Fig. 12. As observed from Fig. 12(a), the surge amplitude corresponding to the natural frequency of the surge mode of the IFES is much smaller than that of the FWT. It means that the response from the surge mode is significantly mitigated by the tidal turbines. The contribution of the surge mode to the heave motion is also reduced as indicated by Fig. 12(b). It is noted that the discrepancy in the amplitudes at other frequencies of the IFES and FWT is insignificant. Since the platform pitch is mainly influenced by the wind loading, the spectral responses of the platform pitch of the IFES and FWT are similar.
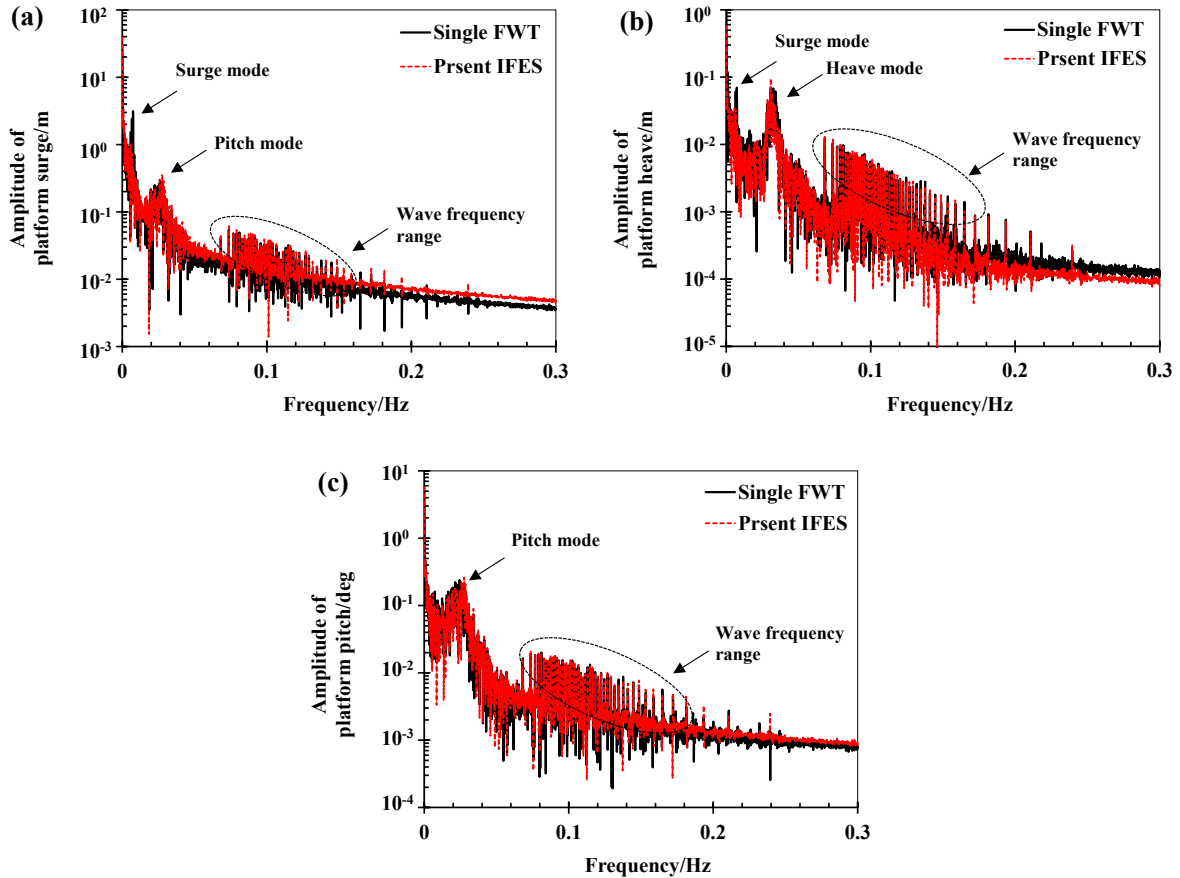
Fig. 12: Spectral responses of the platform under LC2. (a) surge, (b) heave and (c) pitch.

The statistical results of the platform motions are given in Table 6. Similar to the results under LC2, the maximum surge motion of the IFES is larger than that of the FWT under both LC1 and LC3 due to the additionally considerable thrusts produced by the tidal turbines. For the same reason, the standard deviations are smaller. Under LC1, the surge standard deviations of the IFES and FWT are 1.55 m and 2.49 m, respectively. It means that the tidal turbines mitigate the surge fluctuation by 37.5%. Reductions of 57.2% and 42.1% on the surge standard deviation are achieved under LC2 and LC3, respectively. It is anticipated that the fluctuation of the tension in a mooring line will decrease due to the tidal turbines under all the LCs.

Table 6: Statistical platform responses of the IFES and FWT (during 400 s ~ 4600s)

	Surge/m	Heave/m	Pitch/degree

		IFES	FWT	IFES	FWT	IFES	FWT
	Max	24.67	19.93	0.136	1.395	4.162	4.137
LC1	Mean	20.49	13.72	-0.114	1.129	2.877	2.802
	Std.dev	**1.55**	**2.49**	0.101	0.095	0.419	0.448
	Max	33.54	32.58	0.436	1.803	7.709	7.705
LC2	Mean	28.13	20.02	-0.425	0.926	4.171	4.101
	Std.dev	**2.29**	**5.36**	0.217	0.212	1.151	1.207
	Max	30.30	23.66	0.446	1.850	6.510	6.331
LC3	Mean	23.57	13.67	-0.200	1.117	3.026	2.842
	Std.dev	**1.90**	**3.27**	0.226	0.212	1.182	1.112

570

5.4 Tension in mooring lines

Fig. 13 presents the fairlead tension of each mooring line of the IFES and FWT under LC2. As expected, the fluctuation of tension in the mooring lines of the IFES is smaller than that of the FWT due to the smaller variation range of the surge motion. As the IFES suffers an additionally considerable thrust generated by the tidal turbines, its equilibrium position is relatively farther than that of the FWT. Consequently, compared with the single FWT, the mooring line #1 placed in the downwind direction is in a looser state, while the stretched lengths of the upwind mooring lines (#2 and #3) are larger. As a result, the mean tension in mooring line #1 of the IFES is smaller compared to the results of the FWT, while the mooring lines #2 and #3 have a larger average tension.
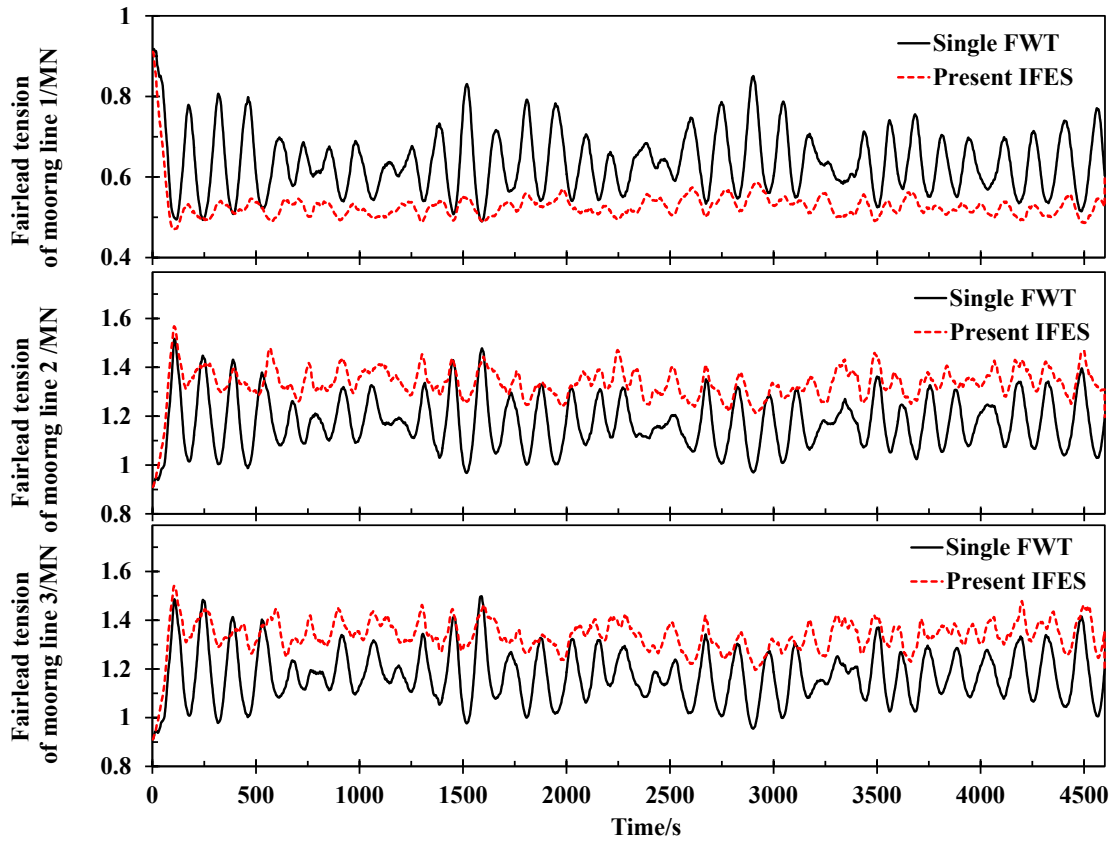
Fig. 13: Fairlead tension in the mooring lines of the IFES and FWT under LC2

The mean values and standard deviations of the fairlead tension in the mooring lines of the IFES and FWT under all the three LCs are presented in Table 7. Similar to the results under LC2, the average tension in mooring line #1 of the IFES is smaller than that of the FWT under both LC1 and LC3. In addition, the standard deviation of the tension in mooring line is significantly decreased by the tidal turbines. For the upwind mooring lines, the mean tension increases and the standard deviation of the tension decreases due to the presence of the tidal turbines. More specifically, the mean tensions in mooring line #2 of the IFES and FWT under LC 1 are 1196.0 kN and 1083.2 kN, respectively. The corresponding standard deviations of the tensions are 28.1 kN and 40.3 kN, respectively. The mean tension increases by 10.4% while the standard deviation decreases by 30.4%. Similar phenomena are observed for LC2 and LC3. The enhancements on the mean tension in mooring line #2 under LC2 and LC3 are 162.9 kN

595   and 177.7 kN, respectively, equivalent to increase of 13.8% and 16.3%. Meanwhile, the

596   standard deviations of the tension in mooring line #2 under LC2 and LC3 decrease by 53.3%

597   and 39.3%, respectively. The statistical results indicate that the load in a downwind mooring

598   line is mitigated, while the loads in the upwind mooring lines are enhanced by the tidal turbines.

599   It is anticipated that the service lifetime of the downwind mooring line will be extended due to

600   the smaller mean load and fluctuation. However, the influence on the fatigue damage of the

601   upwind mooring lines requires a further investigation, since the mean value of the tension

602   increases but the standard deviation significantly decreases.

603

604   Table 7: Mean value and standard deviation of the fairlead tension of the mooring lines

		Mooring line #1/kN		Mooring line #2/kN		Mooring line #3/kN	
		IFES	FWT	IFES	FWT	IFES	FWT
LC1	Mean	593.1	700.9	1196.0	1083.2	1196.4	1082.9
	Std.dev	16.4	38.8	28.1	40.3	28.1	41.3
LC2	Mean	522.9	632.2	1340.7	1177.8	1346.0	1180.6
	Std.dev	17.3	72.3	49.2	105.4	49.7	103.5
LC3	Mean	557.7	703.7	1265.3	1087.6	1256.0	1077.1
	Std.dev	13.5	50.1	33.2	54.7	33.6	54.7

605

606 *5.5 Power production*

607   The generator power of the IFES and FWT under LC2 is presented in Fig. 14. As indicated

608   in the previously presented results, the tidal turbines have a slight influence on the aerodynamic

609   performance of the wind turbine. Therefore, the generator power of the IFES contributed by

610   the wind turbine is similar to that of the single FWT. The average generator powers of the IFES

611   and FWT are 4773.7 kW and 4777.2 kW, respectively. The inflow current speed at the MSL is

612   1.1 m/s in LC2. It means that the constant inflow current speed at the depth of 46.5 m is 1.08

613   m. The corresponding design power of the tidal turbine is 88.4 kW. The dynamic inflow due

614   to the platform motions affects the actual generator power of the tidal turbines. The average

615   power of the two tidal turbines is 183.2 kW that is slightly higher than the target design power.

616   Compared to a single FWT, the average output power is increased by 3.84% due to the presence
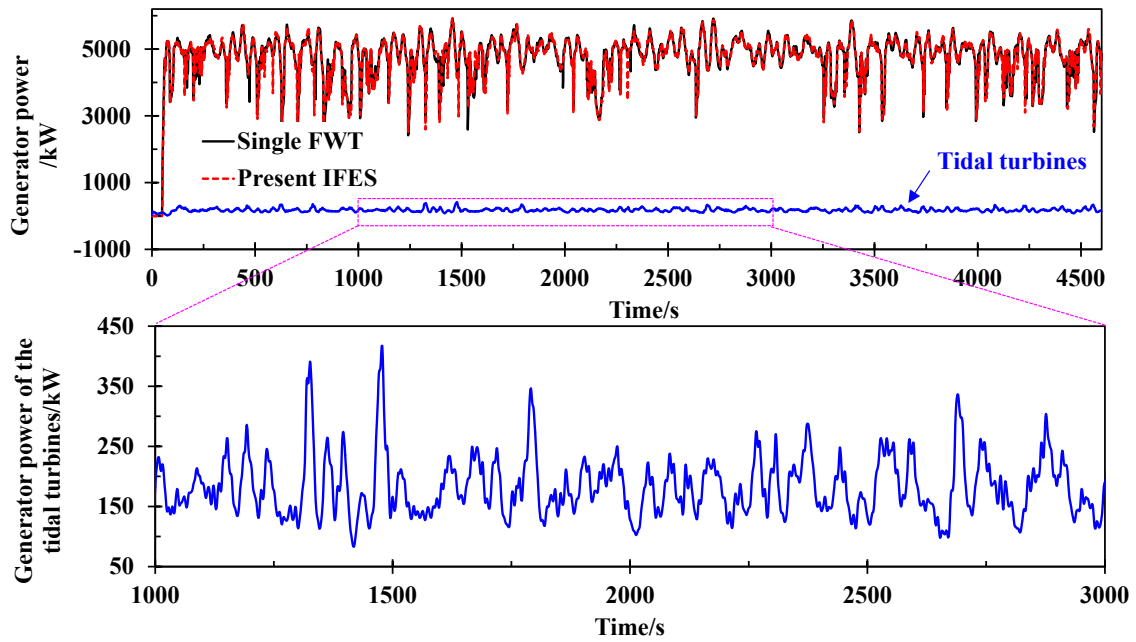
617   of the tidal turbines under LC2.

619   Fig. 14: Generator power of the IFES and FWT under LC2

621   The presence of the tidal turbines has a slight influence on the power production of the

622   wind turbine for the examined LCs, as indicated by Table 8. The results indicate that the total

623   power production is increased by 3.84% to 6.46% due to additional tidal turbines. Although

624   the wind power of the IFES is decreased by 10.1 kW compared to the single FWT, the tidal

625   turbines provides an additional power production of 135.1 kW. As a result, the total power of

626   the IFES is increased by 6.46%. It is also found that the total power production increases by

627   237 kW under LC3, equivalent to an enhancement of 4.74%.

628   Table 8: Average power of the wind and tidal turbines under the examined LCs

	IFES/kW			FWT/kW	Error
	Wind	Tidal	Total	Total	
LC1	1923.1	135.1	2058.2	1933.2	6.46%
LC2	4773.7	183.3	4957.0	4777.2	3.84%
LC3	4998.9	237.0	5235.9	4998.7	4.74%

The average power output of the FWT and IFES including the contributions of the tidal turbines under the three LCs are presented in Fig. 15. The average power generation of the IFES is higher than the one of the FWT for each LC. It means that the tidal turbine is beneficial in enhancing the total power production of the floating wind energy system.
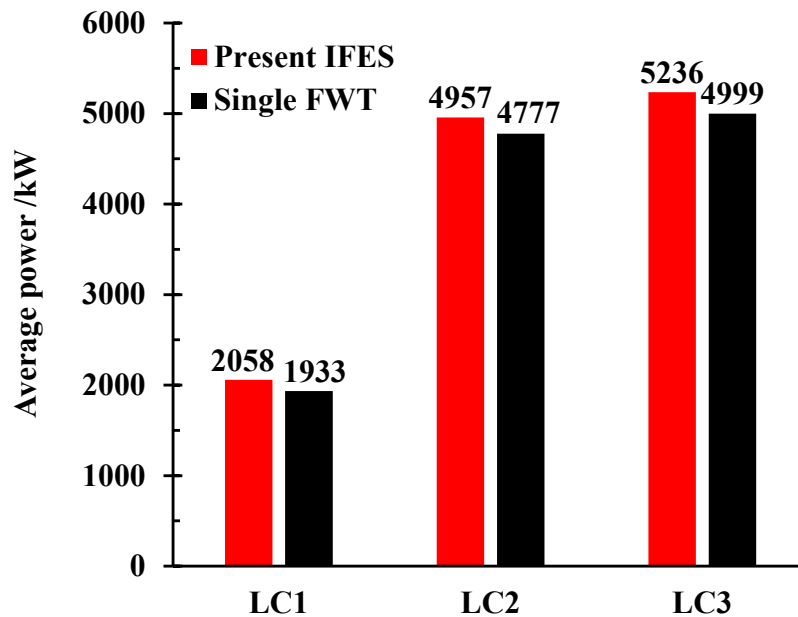

Fig. 15: Average power outputs of the IFES and FWT under the three LCs

6 Conclusions

This study proposed an integrated floating energy system by combining two 550 kW tidal turbines with a 5 MW wind turbine supported by a spar platform. A novel fully coupled numerical tool is developed by implementing the aero-servo-elastic simulation capabilities within the commercial hydrodynamic analysis software package, AQWA. In addition, the AeroDyn program is integrated with the coupled tool to evaluate performance of the tidal turbines. A torque-pitch controller is implemented within the coupled tool for the tidal turbines operating under dynamic inflow conditions due to the platform motions. Numerical results

645 from OpenFAST and experimental data from model tests are used to verify the accuracy of the

646 fully coupled model in predicting dynamic responses of a FWT and tidal turbines. The

647 aerodynamic performance of the rotor, and dynamic responses of the blade, platform and

648 mooring system of the IFES under different LCs are obtained using the coupled tool. The main

649 conclusions of this study are listed as follows:

650 (1) A novel fully coupled aero-hydro-servo-elastic tool based on AQWA and AeroDyn

651 program is developed for dynamic analysis of the IFES concept. The comparisons against

652 OpenFAST and model tests have validated the accuracy of the coupled tool in predicting

653 dynamic responses of a hybrid floating energy concept subjected to wind and wave loadings.

654 The DLL is capable of examining aero-servo-elastic coupled effects of FWTs and it has been

655 released to the public. Details of the open source code can be found in Appendix B.

656 (2) The tidal turbines have insignificant influences on the blade-tip deflection and rotor

657 thrust of the wind turbine. The transient behavior of the platform is improved due to the

658 presence of the tidal turbines which provide a considerable damping against the wind turbine

659 moving towards the upwind direction. The IFES has similar dynamic responses of blades and

660 aerodynamic performance to those of a single FWT, while the hydrodynamic performance is

661 better.

662 (3) The downwind mooring line of the IFES has a smaller mean fairlead tension compared

663 to the FWT, while the fluctuation range is much smaller. The fatigue damage is anticipated to

664 be reduced by the presence of the tidal turbines. Although the mean tensions in the upwind

665 mooring lines of the IFES are larger than those of a FWT, the standard deviations are much

666 smaller. The standard deviation of the tension in an upwind mooring line decreases by 30.4%

667 to 53.3% depending on the environmental conditions.

668 (4) The average power generation of the IFES is higher than the one of the FWT for each

669 of the examined load cases. An enhancement of up to 6.46% is achieved on the overall power

670 production due to the tidal turbines. The results confirm that the IFES concept is beneficial in

671 enhancing total power production without weakening the dynamic performance of a FWT.

672

Appendix A: Implementation of the controller for the tidal turbine

674   This study employs the control algorithm developed by Jonkman for the NREL 5 MW

675 wind turbine in implementing the torque-pitch controller for the tidal turbine. The torque-pitch

676 controller consists of a simple partial-load controller and a proportional-integral (PI) controller.

677 The partial-load controller defines the torque-speed curve when the output power is smaller

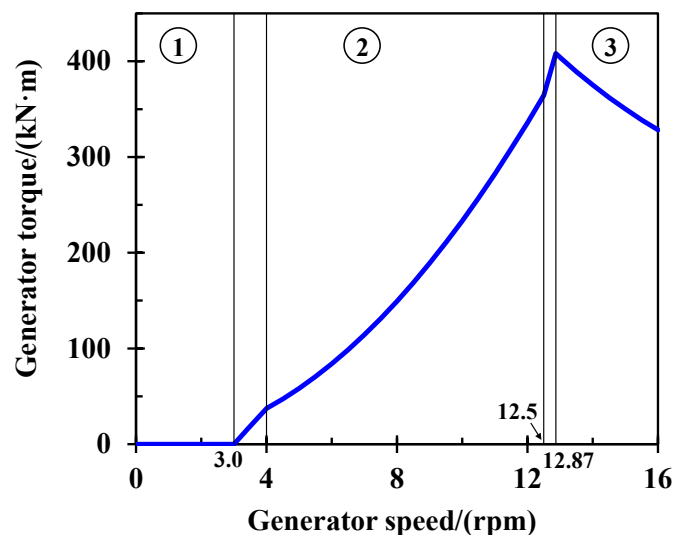678 than the rated power as shown in Fig. 16. The gearbox ratio is assumed to be 1 for simplicity.

680 Fig. 16: Torque versus rotor speed of the controller

681   In region 1, the generator torque is 0. The cut-in rotor speed for outputting power is chosen

682 as 3 rpm. In region 2, the torque is equal to the square of the generator speed. The tidal turbine

683 operates in its best TSR of 6.98. The quadratic coefficient is 2333.4 $Nm/(rpm)^2$. The starting

684 and ending limits of region 2 are chosen as 4 rpm and 12.5 rpm. The starting generator speed

685 of region 3 is selected as 99% of the rated speed. Once the generator speed exceeds the limit,

686 the PI controller takes over in region 3 where the target output power remains constantly being

687 the rated power.

688   In region 3, a PI controller is activated to adjust blade pitch angle as follows:

689
$$\Delta\theta = K_P \Delta\Omega + K_I \int_0^t \Delta\Omega \, \mathrm{d}t \tag{22}$$

690 where $\Delta\theta$ and $\Delta\Omega$ are the perturbations of the blade pitch angle and generator speed; K_P

691 and K_I are the proportional and integral gains, respectively.

692   Based on the power performance of the tidal turbine, K_P and K_I corresponding to 0

693 degree blade pitch are obtained with values of 39.42 rad·s/rad and 16.89 rad/rad, respectively.

694 The linear adjustment coefficient η of the PI gains for a specific blade pitch angle θ is given

695 as:

696
$$\eta = 1/(1 + \theta/\psi) \tag{23}$$

697 where ψ is 0.00345 rad.

698   The main parameters of the controller are given in Table 9. Fig. 17 presents the generator

699 power, rotor speed and blade pitch of the tidal turbine under an unsteady inflow condition. The

700 inflow current speed increases gradually from 0.5 m/s to 3.0 m/s over the simulation. The

701 results shown in Fig. 17 indicate that the controller implemented in this study is effective to

702 adjust rotor speed and blade-pitch of the tidal turbines under dynamic inflow current conditions.

703   Table 9: Main parameters of the controller

Value	Variable	Description
1.570796	CornerFreq	Corner frequency (-3dB point) in the low-pass filter, rad/s.
0.0001	PC_DT	Communication interval for pitch controller, s.
16.89436	PC_KI	Integral gain for pitch controller at rated pitch (zero), (-).
0.003452	PC_KK	Gains adjustment coefficient.
39.42017	PC_KP	Proportional gain for Pitch controller at rated Pitch (zero), s.
1.570796	PC_MaxPit	Maximum pitch setting in pitch controller, rad.
0.139626	PC_MaxRat	Maximum pitch rate (in absolute value) in pitch controller, rad/s.
0.0	PC_MinPit	Minimum pitch setting in pitch controller, rad.
1.361357	PC_RefSpd	Desired (reference) HSS speed for pitch controller, rad/s.
0.314159	VS_CtInSp	Transitional generator speed (HSS side) between regions 1 and 1 1/2, rad/s.
0.0001	VS_DT	Communication interval for torque controller, s.
80000	VS_MaxRat	Maximum torque rate (in absolute value) in torque controller, N-m/s.
484810.4	VS_MaxTq	Maximum generator torque in Region 3 (HSS side), N-m.
212779.5	VS_Rgn2K	Generator torque constant in Region 2 (HSS side), N-m/(rad/s)^2.
0.418879	VS_Rgn2Sp	Transitional generator speed (HSS side) between regions 1 1/2 and 2, rad/s.
0.017453	VS_Rgn3MP	Minimum pitch angle in region 3 regardless of the generator speed, rad.
1.347743	VS_RtGnSp	Rated generator speed (HSS side), rad/s.
550000	VS_RtPwr	Rated generator power in Region 3, Watts.
10	VS_SlPc	Rated generator slip percentage in Region 2 1/2, %.

704

705
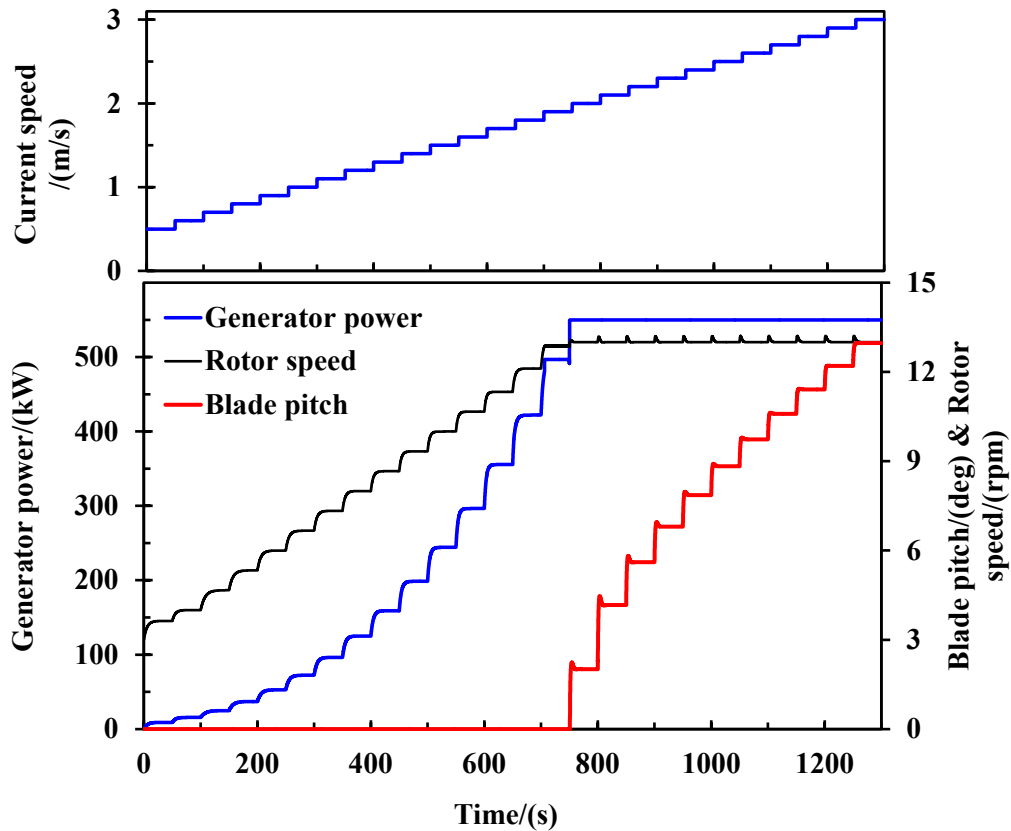
Fig. 17: Controller performance under an unsteady inflow condition

Appendix B: Public release of the fully coupled model

The DLL used in this study, which is capable of performing a fully coupled analysis of FWTs using AQWA, is released to the public on GitHub and can be accessed via the link: https://github.com/yang7857854/F2A. The source code and a user manual of F2A have been uploaded in the repository.

References

[1] DNV-GL. (2019), Energy transition outlook 2019: A global and regional forecast to 2050. *Det Norske Veritas - Germanischer Lloyd report*, 2019

[2] Driscoll, F., Jonkman, J., Robertson, A., Sirnivas, S., Skaare, B., & Nielsen, F. G. (2016). Validation of a FAST model of the statoil-hywind demo floating wind turbine. *Energy Procedia*, 94(NREL/JA-5000-66650).

[3] Jonkman, J. (2010). Definition of the Floating System for Phase IV of OC3. *National Renewable Energy Laboratory (NREL), Technical report (*No. NREL/TP-500-47535t*)*, Colorado, United States.

[4] Karimirad, M., & Moan, T. (2011). Wave-and wind-induced dynamic response of a spar-type offshore wind turbine. *Journal of waterway, port, coastal, and ocean engineering*, 138(1), 9-20.

[5] Yu, M., Hu, Z. Q., & Xiao, L. F. (2015). Wind-wave induced dynamic response analysis for motions and mooring loads of a spar-type offshore floating wind turbine. *Journal of Hydrodynamics*, 26(6), 865-874.

[6] Yue, M., Liu, Q., Li, C., Ding, Q., Cheng, S., & Zhu, H. (2020). Effects of heave plate on dynamic response of floating wind turbine Spar platform under the coupling effect of wind and wave. *Ocean Engineering*, 201, 107103.

[7] Ahn, H. J., & Shin, H. (2019). Model test and numerical simulation of OC3 spar type floating offshore wind turbine. *International Journal of Naval Architecture and Ocean Engineering*, 11(1), 1-10.

[8] Lin, Y. H., Hsu, C. L., & Kao, S. H. (2019). Hydrodynamics of the wind float OC3-Hywind with mooring loads estimated by the modular system. J*ournal of Marine Science and Technology*, 24(1), 237-248.

[9] Lyu, G., Zhang, H., & Li, J. (2019). Effects of incident wind/wave directions on dynamic response of a SPAR-type floating offshore wind turbine system. *Acta Mechanica Sinica*, 35(5), 954-963.

[10] Robertson, A., Jonkman, J., Masciola, M., Song, H., Goupee, A., Coulling, A., & Luan, C. (2014). Definition of the semisubmersible floating system for phase II of OC4. *National Renewable Energy Laboratory (NREL), Technical report (No. NREL/TP-5000-60601)*, Colorado, United States.

[11] Matha, D. (2010). Model development and loads analysis of an offshore wind turbine on a tension leg platform with a comparison to other floating turbine concepts. *National Renewable Energy Laboratory (NREL), Technical report (No. NREL/SR-500-4589)*, Colorado, United States.

[12] Jonkman, J. M., & Matha, D. (2011). Dynamics of offshore floating wind turbines—analysis of three concepts. *Wind Energy*, 14(4), 557-569.

758 [13] Yuce, M. I., & Muratoglu, A. (2015). Hydrokinetic energy conversion systems: A
759 technology status review. *Renewable and Sustainable Energy Reviews*, 43, 72-82.

760 [14] Patel, V., Eldho, T. I., & Prabhu, S. V. (2017). Experimental investigations on Darrieus
761 straight blade turbine for tidal current application and parametric optimization for hydro
762 farm arrangement. *International journal of marine energy*, 17, 110-135.

763 [15] Patel, V., Eldho, T. I., & Prabhu, S. V. (2019). Performance enhancement of a Darrieus
764 hydrokinetic turbine with the blocking of a specific flow region for optimum use of
765 hydropower. *Renewable Energy*, 135, 1144-1156.

766 [16] Blackmore, T., Myers, L. E., & Bahaj, A. S. (2016). Effects of turbulence on tidal turbines:
767 Implications to performance, blade loads, and condition monitoring. *International Journal
768 of Marine Energy*, 14, 1-26.

769 [17] Scarlett, G. T., & Viola, I. M. (2020). Unsteady hydrodynamics of tidal turbine blades.
770 *Renewable Energy*, 146, 843-855.

771 [18] Bahaj, A. S., Batten, W. M. J., & McCann, G. (2007). Experimental verifications of
772 numerical predictions for the hydrodynamic performance of horizontal axis marine
773 current turbines. *Renewable energy*, 32(15), 2479-2490.

774 [19] Zhang, L., Wang, S. Q., Sheng, Q. H., Jing, F. M., & Ma, Y. (2015). The effects of surge
775 motion of the floating platform on hydrodynamics performance of horizontal-axis tidal
776 current turbine. *Renewable energy*, 74, 796-802.

777 [20] Patel, V., Bhat, G., Eldho, T. I., & Prabhu, S. V. (2017). Influence of overlap ratio and
778 aspect ratio on the performance of Savonius hydrokinetic turbine. *International Journal of
779 Energy Research*, 41(6), 829-844.

780 [21] Patel, V., Eldho, T. I., & Prabhu, S. V. (2018). Theoretical study on the prediction of the
781 hydrodynamic performance of a Savonius turbine based on stagnation pressure and
782 impulse momentum principle. *Energy Conversion and Management*, 168, 545-563.

783 [22] Muliawan, M. J., Karimirad, M., & Moan, T. (2013). Dynamic response and power
784 performance of a combined spar-type floating wind turbine and coaxial floating wave
785 energy converter. *Renewable Energy*, 50, 47-57.

786 [23] Wan, L., Gao, Z., & Moan, T. (2015). Experimental and numerical study of hydrodynamic
787 responses of a combined wind and wave energy converter concept in survival modes.
788 *Coastal Engineering*, 104, 151-169.

789 [24] Michailides, C., Gao, Z., & Moan, T. (2016). Experimental study of the functionality of a
790 semisubmersible wind turbine combined with flap-type Wave Energy Converters.
791 *Renewable Energy*, 93, 675-690.

792 [25] Michailides, C., Gao, Z., & Moan, T. (2016). Experimental and numerical study of the
793 response of the offshore combined wind/wave energy concept SFC in extreme
794 environmental conditions. *Marine Structures*, 50, 35-54.

795 [26] Michele, S., Renzi, E., Perez-Collazo, C., Greaves, D., & Iglesias, G. (2019). Power
796 extraction in regular and random waves from an OWC in hybrid wind-wave energy
797 systems. *Ocean Engineering*, 191, 106519.

798 [27] Hallak, T. S., Gaspar, J. F., Kamarlouei, M., Calvário, M., Mendes, M. J., Thiebaut, F., &
799 Guedes Soares, C. (2018). Numerical and experimental analysis of a hybrid wind-wave
800 offshore floating platform's hull. *In ASME 2018 37th International Conference on Ocean,
801 Offshore and Arctic Engineering*, Madrid, Spain.

802 [28] Li, L., Gao, Y., Yuan, Z., Day, S., & Hu, Z. (2018). Dynamic response and power
803 production of a floating integrated wind, wave and tidal energy system. *Renewable energy*,
804 116, 412-422.

[29] Li, L., Cheng, Z., Yuan, Z., & Gao, Y. (2018). Short-term extreme response and fatigue damage of an integrated offshore renewable energy system. *Renewable Energy*, 126, 617-629.

[30] Li, L., Yuan, Z. M., Gao, Y., Zhang, X., & Tezdogan, T. (2019). Investigation on long-term extreme response of an integrated offshore renewable energy device with a modified environmental contour method. *Renewable energy*, 132, 33-42.

[31] Jonkman, J., Butterfield, S., Musial, W., & Scott, G. (2009). Definition of a 5-MW reference wind turbine for offshore system development. *National Renewable Energy Laboratory (NREL), Technical report (No. NREL/TP-500-38060)*, Colorado, United States.

[32] Neary, V. S., Lawson, M., Previsic, M., Copping, A., Hallett, K. C., LaBonte, A., & Murray, D. (2014). Methodology for Design and Economic Analysis of Marine Energy Conversion (MEC) Technologies. *Sandia National Laboratory, Technical report (No. SAND2014-3561C)*, New Mexico, United States.

[33] Moriarty, P. J., & Hansen, A. C. (2005). AeroDyn theory manual. *National Renewable Energy Laboratory (NREL), Technical report (No. NREL/TP-500-36881)*, Colorado, United States.

[34] Jonkman, J. M., Hayman, G. J., Jonkman, B. J., Damiani, R. R., & Murray, R. E. (2015). AeroDyn v15 User's Guide and Theory Manual. *National Renewable Energy Laboratory (NREL)*, Colorado, United States.

[35] Yang, Y., Li, C., Zhang, W., Yang, J., Ye, Z., Miao, W., & Ye, K. (2016). A multi-objective optimization for HAWT blades design by considering structural strength. *Journal of Mechanical Science and Technology*, 30(8), 3693-3703.

[36] Jonkman, J. M. (2003). Modeling of the UAE Wind Turbine for Refinement of FAST {_} AD. *National Renewable Energy Laboratory (NREL), Technical report (No. NREL/TP-500-34755)*, Colorado, United States.

[37] Jonkman, J., & Buhl, M. (2004, January). New developments for the NWTC's fast aeroelastic HAWT simulator. In 42nd AIAA Aerospace Sciences Meeting and Exhibit, Nevada, United States.

[38] Bahaj, A. S., Molland, A. F., Chaplin, J. R., & Batten, W. M. J. (2007). Power and thrust measurements of marine current turbines under various hydrodynamic flow conditions in a cavitation tunnel and a towing tank. *Renewable energy*, 32(3), 407-426.

[39] Doman, D. A., Murray, R. E., Pegg, M. J., Gracie, K., Johnstone, C. M., & Nevalainen, T. (2015). Tow-tank testing of a 1/20th scale horizontal axis tidal turbine with uncertainty analysis. *International Journal of Marine Energy*, 11, 105-119.

[40] Jonkman, J., & Musial, W. (2010). Offshore code comparison collaboration (OC3) for IEA Wind Task 23 offshore wind technology and deployment. *National Renewable Energy Laboratory (NREL), Technical report (No. NREL/ TP-5000-48191)*, Colorado, United States.

[41] Robertson, A. N., Wendt, F., Jonkman, J. M., Popko, W., Dagher, H., Gueydon, S., ... & Soares, C. G. (2017). OC5 project phase II: validation of global loads of the DeepCwind floating semisubmersible wind turbine. *Energy Procedia*, 137, 38-57.

[42] Stewart, G. M., Robertson, A., Jonkman, J., & Lackner, M. A. (2016). The creation of a comprehensive metocean data set for offshore wind turbine simulations. *Wind Energy*, 19(6), 1151-1159.

[43] Jonkman, Bonnie J. (2009). TurbSim user's guide: Version 1.50. Jonkman, J. M., & Buhl Jr, M. L. (2005). FAST user's guide. *National Renewable Energy Laboratory (NREL), Technical Reports (No. NREL/TP-500-46198)*, Golden, United States.